

1 <https://doi.org/10.1016/j.enggeo.2021.106272>

2

3 **Pellets/block bentonite barriers: laboratory study of their evolution upon**
4 **hydration**

5 María Victoria Villar^a, Rubén Javier Iglesias, Carlos Gutiérrez-Álvarez, Beatriz Carbonell

6 Centro de Investigaciones Energéticas, Medioambientales y Tecnológicas (CIEMAT), Avd.

7 Complutense 40, 28040 Madrid, Spain

8 ^acorresponding author: mv.villar@ciemat.es, +34 913466391

9 **1 Introduction**

10 The backfilling and sealing of deposition galleries or holes and access galleries and shafts is an
11 important part of the nuclear waste underground repository design. Openings created during the
12 construction of the repository are potential preferential pathways for water, gas and radionuclides
13 migration, and have to be effectively sealed. Bentonite or bentonite-based mixtures have been
14 proposed as backfill and sealing materials for their low permeability, high swelling capacity and high
15 retention capacity. To enhance these properties bentonite has to be compacted, and dry density
16 values of between 1.45 and 1.65 g/cm³ are usually considered appropriate to ensure the main safety
17 functions of the clay barrier (Sellin and Leupin 2013). The design of clay barriers has been mainly
18 based on using blocks of compacted bentonite and for this reason these materials have been widely
19 characterised in the form of high-density pre-compacted blocks, which have also been used in large-
20 scale experiments (e.g. Dixon et al. 2002, ENRESA 2006, SKB 2010).

21 The use of high-density bentonite pellets (combined or not with powdered bentonite) as barrier
22 material was also proposed several decades ago (Salo & Kukkola 1989, Volckaert et al. 1996). The

23 manufacturing of high-density pellets usually involves the pre-heating of bentonite powder so that a
24 drier and more compressible material can be produced and compacted. The advantage of this
25 material is that it is easy to manufacture and install: the bentonite pellets can be emplaced using
26 auger discharge tubes or even pneumatic projection techniques. Thus, the backfilling operation
27 becomes an easier and potentially robotised procedure. The initial works using pellets considered
28 vertical emplacement of the canister. This was the case of the large-scale demonstration experiment
29 RESEAL, where a mixture of high-density bentonite pellets and bentonite powder was used to backfill
30 a vertical shaft at the Hades Underground Research Facility in Mol, Belgium (Volckaert et al. 2000,
31 van Geet et al. 2009). The pellets used in that project were all manufactured in the same size and
32 shape from FoCa bentonite, and the effect of the pellet/powder ratio on the mixture properties was
33 also tested in the laboratory (e.g. Imbert et al. 2002). More recently, the Institut de Radioprotection
34 et de Sûreté Nucléaire (IRSN, France) studied the use of MX-80 bentonite pellets/powder mixtures as
35 backfill material, including both laboratory (Molinero Guerra 2018) and in situ investigations
36 performed at the Tournemire Underground Research Laboratory (URL, France,
37 [https://www.irsn.fr/dechets/recherche/programmes/scellement-stockage/Pages/essais-in-](https://www.irsn.fr/dechets/recherche/programmes/scellement-stockage/Pages/essais-in-situ.aspx)
38 [situ.aspx](https://www.irsn.fr/dechets/recherche/programmes/scellement-stockage/Pages/essais-in-situ.aspx)), whereas the Full-Scale Seal test (FSS), run by the French nuclear waste agency (ANDRA),
39 tested this kind of mixtures in a surface facility as a seal for repository concepts both for high and
40 intermediate-level radioactive wastes (Bosgiraud and Foin 2016). The use of regular pellets combined
41 with powder is currently being tested in the framework of the VSEAL project to backfill vertical shafts
42 at the Tournemire facility (e.g. Alcantara et al. 2020).

43 However, in the case of horizontal placement, a rigid support for the canister is needed, what can be
44 achieved by the combined use of a lower bed made of highly compacted bentonite blocks in which
45 the waste canister rests and an upper buffer made of granular bentonite material (GBM, i.e. pellets).
46 This disposal concept has been adopted by the Swiss waste management agency, and is described in
47 detail in NAGRA (2019) and references therein. The pellets/blocks construction concept was initially

48 demonstrated in the large-scale Engineered Barrier Emplacement Experiment (EB), carried out at the
49 Mont Terri URL, which is excavated in Opalinus Clay, using FEBEX bentonite to construct the two-
50 component barrier (ENRESA 2005, García-Siñeriz et al. 2015). Afterwards, other large-scale
51 experiments have been launched at the Mont Terri URL (e.g. HE-E and FE, using MX-80 bentonite) to
52 investigate the performance of this type of material under actual operational conditions (Gaus et al.
53 2014, Müller et al. 2017). In all the projects mentioned in this paragraph, the bentonite pellets had
54 irregular shapes and different sizes (15-0.4 mm), and they were combined in granulometric curves
55 optimized to give as high as possible overall dry densities avoiding at the same time excessive
56 segregation.

57 The blocks used to support the containers will be manufactured from the bentonite with hygroscopic
58 water content (or higher than hygroscopic in some disposal concepts) compacted at a high dry
59 density. In contrast, the initial water content of the pellets will be low (because of the drying process
60 prior to manufacturing), and they will be poured by auger conveyors or projected. As a result, the
61 density of the GBM once emplaced will be much lower than that of the compacted blocks.
62 Furthermore, the two materials will also be very different in terms of their pore size distribution,
63 with larger pores expected in the GBM part (e.g. Hoffmann et al. 2007). Hence, it is clear that the
64 combined use of pellets and blocks in the same section of the barrier introduces difficulties in the
65 understanding and modelling of the system performance that have to be addressed. So far there is
66 just a large-scale in situ test with a two-component barrier already dismantled (the EB test at Mont
67 Terri mentioned above). The more relevant observation obtained in the dismantling of the test was
68 the considerable homogenization of the dry density of blocks and pellets along a vertical section,
69 although differences in dry density persisted, with the blocks still having overall higher dry density
70 than the GBM (García-Siñeriz et al. 2015, Gens et al. 2021).

71 In this context, the overall objective of the BEACON (Bentonite Mechanical Evolution) project was to
72 evaluate the consequences of heterogeneities on the performance of bentonite barriers in geological

73 repositories for high-level radioactive waste. Although the bentonite buffer shows a natural tendency
74 towards homogenisation, long-term observations both in large-scale and in laboratory tests revealed
75 that a degree of heterogeneity may persist (e.g. Villar et al. 2020, Bernachy-Barbe et al. 2020). In this
76 respect, CIEMAT carried out in the framework of this project a series of tests in cells to evaluate one
77 of the sources of bentonite heterogeneity: the combination in the same barrier of pellets and blocks
78 of compacted bentonite, whose initial dry densities and structures noticeably differ. The aim of this
79 investigation was to obtain qualitative and quantitative information about the evolution, at
80 laboratory scale, of initially inhomogeneous bentonite samples (pellets/blocks) upon hydration under
81 isothermal conditions. Both in the laboratory and in the real case, this evolution might be affected by
82 the characteristics of the barrier system (the particular dry density and water content of each barrier
83 component as well as their sizes) and by the boundary conditions, such as the existence of gaps,
84 temperature and water salinity and availability. In the present research two factors potentially
85 affecting the mechanical evolution of a two-component barrier were analysed: water availability and
86 barrier configuration. Thus, the tests were performed either under constant pressure conditions,
87 simulating a repository excavated in crystalline host rock with plenty of water, such as the
88 underground laboratory of Grimsel (<https://www.grimsel.com/>), or under low water inflow rate,
89 simulating a repository with scarce water availability, which would be the case of clay host rocks
90 (Grambow 2016), such as the underground laboratory in Mont Terri (<https://www.mont-terri.ch/>).
91 An additional variable analysed in this work was the influence of hydrating through the pellets or the
92 block part.

93 To date no tests analysing the hydro-mechanical behaviour of two-component bentonite samples in
94 the laboratory have been published, although Martikainen et al. (2018) performed two similar tests
95 in terms of geometry that were briefly reported and modeled by several groups in Talandier (2019)
96 and Abed and Solowski (2019). Smaller oedometric tests (height 5 cm, diameter 6 cm) in which the
97 two components were blocks of different dry density or pellets and powder were performed by the

98 French Alternative Energies and Atomic Energy Commission (CEA) in the context of the Beacon
99 project (Baryla et al., 2019, Bernachy-Barbe, 2021). Exercises performed to model tests involving
100 saturation of two-component barriers highlighted the fact that the partition between micro and
101 macro porosity was different for the two bentonite materials (Talandier 2019). The conclusion was
102 that double porosity models appear very suitable to simulate the mechanical behaviour of bentonite
103 compacted blocks, bentonite pellets and their combination in a single section of the engineered
104 barrier. More recently, triple porosity models considering inter-pellet pore space, void space
105 between clay aggregates inside pellets and space inside aggregates, have been proposed to model
106 the hydro-mechanical behaviour of pellets/powder mixtures (Navarro et al. 2020).

107 **2 Material and methods**

108 Isochoric infiltration tests were performed in two-component samples, half of them consisting of a
109 bentonite compacted block and the other half of a pellet mixture. Two types of cells were used: a
110 large-scale oedometer (MGR) and a transparent cell (CW). In most tests the lower half of the cell was
111 filled with bentonite pellets with an average dry density close to 1.30 g/cm^3 and the upper part by a
112 1.60 g/cm^3 bentonite block (in two tests the placement was in reverse). In all cases hydration with
113 deionised water took place through the bottom at ambient temperature. These kinds of tests were
114 complementary: whereas MGR tests provided quantitative data, the information provided by the CW
115 test was mostly visual and qualitative.

116 **2.1 Material**

117 The material used in the laboratory tests was a bentonite extracted from the Cortijo de Archidona
118 quarry (Almería, Spain) at two different moments. The first batch, known as FEBEX bentonite, was

119 extracted in 1995 and is a granulate used to obtain the compacted blocks. The second batch was
120 extracted in 2001 and was used to manufacture the pellets.

121 The FEBEX bentonite is a 900-t batch of bentonite processed in 1996 for the FEBEX project. The
122 processing consisted in homogenisation, air-drying and manual removing of volcanic pebbles on site
123 and, at the factory, crumbling, drying in a rotary oven at temperatures between 50 and 60°C to a
124 water content of around 13%, and sieving through a 5-mm mesh. The physico-chemical properties of
125 the FEBEX bentonite, as well as its most relevant thermo-hydro-mechanical and geochemical
126 characteristics were reported in ENRESA (2006) and updated in e.g. Villar (2017).

127 The smectite content of the FEBEX bentonite is close to 90 wt.%. The smectitic phases are actually
128 made up of a montmorillonite-illite mixed layer, with 10-15 wt.% of illite layers. Besides, the
129 bentonite contains variable quantities of quartz, plagioclase, K-felspar, calcite, and cristobalite-
130 trydimite. The cation exchange capacity is 98 ± 2 meq/100g, the main exchangeable cations being
131 calcium (35 ± 2 meq/100g), magnesium (31 ± 3 meq/100g) and sodium (27 ± 1 meq/100g). The
132 predominant soluble ions are chloride, sulphate, bicarbonate and sodium.

133 The liquid limit of the bentonite is 102 ± 4 %, the plastic limit 53 ± 3 %, the density of the solid particles
134 2.70 ± 0.04 g/cm³ and 67±3 % of particles are smaller than 2 µm. The hygroscopic water content in
135 equilibrium with the laboratory atmosphere (relative humidity 50±10%, temperature 21±3°C) is
136 13.7±1.3%.

137 The saturated hydraulic conductivity of compacted samples of the FEBEX reference bentonite is
138 exponentially related to their dry density. Two empirical relationships relating hydraulic conductivity
139 (k_w , m/s) to dry density (ρ_d , g/cm³) were obtained for samples permeated with deionised water at
140 room temperature, valid each for a different dry density range (Villar 2002):

141 For $\rho_d > 1.47$ g/cm³: $\log k_w = -2.96 \rho_d - 8.58$ [1]

142 For $\rho_d < 1.47$ g/cm³: $\log k_w = -6.00 \rho_d - 4.09$ [2]

143 The swelling pressure (P_s , MPa) of compacted samples is also exponentially related to the bentonite
144 dry density, according to the empirical expression in Eq. 3 (Villar 2002):

$$145 \ln P_s = 6.77 \rho_d - 9.07 \quad [3]$$

146 Relationships between suction and water content obtained for different bentonite dry densities
147 under isochoric conditions can be found in e.g. Villar et al. (2019). For a sample compacted at dry
148 density 1.6 g/cm^3 with hygroscopic water content the initial suction value would be $\sim 120 \text{ MPa}$.

149 The pellets were prepared for the EB project (ENRESA 2005) using a 100-t batch of bentonite
150 extracted in 2001 also from the Cortijo de Archidona deposit. To manufacture the pellets the
151 bentonite was dried and milled in a multi-step process to produce a fine grade powder with a water
152 content of between 3.0 and 4.5%. Later, a commercial plant with an in-line highly automated
153 briquetting process produced coarse (7-15 mm) and fine (0.05-2 mm) grained materials with dry
154 densities of 2.11 and 2.13 g/cm^3 , respectively (Kennedy et al. 2004). Preliminary mineralogical
155 analyses suggest that the content of smectite of this batch could be lower than in the FEBEX batch,
156 whereas the quartz, calcite and dolomite contents would be higher. The cationic exchange capacity
157 was also checked to be lower (Villar and Gómez-Espina 2012). A detailed hydro-mechanical
158 characterisation of this mixture was performed by Hoffmann (2005).

159 The different grain sizes were kept separated in the laboratory and mixed in the right proportion just
160 before every test, trying to keep a Fuller's curve similar to that used for the EB project, with a
161 maximum diameter of 12.7 mm and a minimum diameter of 0.425 mm , in order to reduce
162 segregation. The precise granulometric distribution used in the laboratory tests is shown in Tab. 1.
163 Except for the two first tests performed (MGR21 and MGR22) no pellets larger than 9.5 mm were
164 used (the laboratory run out of them). In tests MGR23 to MGR27 the pellets were softly dried to a
165 water content closer to the fabrication one (3.5%), because the water content of the pellets had
166 increased during storage to a value of $\sim 10\%$. This resulted in a significant different initial suction

167 between the pellets that were dried and those that were not, 380 vs. 114 MPa (measured with a
168 capacitive sensor).

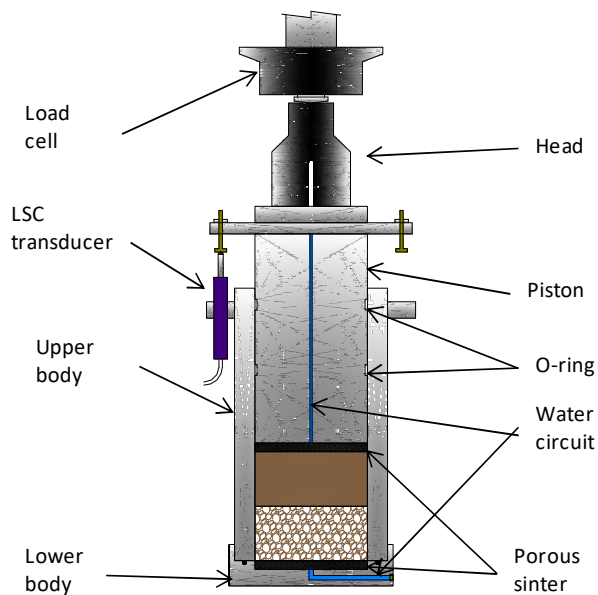
169 **Tab. 1. Granulometric curve of the bentonite pellets used in the tests (MGR and CW)**

| Sieve sizes (mm) | Percentage retained (%) | |
|------------------|-------------------------|---------------|
| | MGR21, MGR22 | Rest of tests |
| 9.5 | 17 | 0 |
| 4.75 | 31 | 37 |
| 2.0 | 26 | 31 |
| 1.18 | 11 | 13 |
| 0.59 | 10 | 12 |
| 0.425 | 5 | 6 |

170

171 **2.2 Tests in large-scale oedometer**

172 The large-scale oedometer consists of a cylindrical body with base and an upper piston that may
173 move along the cylinder (Fig. 1). The body has an inner diameter of 10.0 cm and the length of the
174 sample inside was 10.0 cm. The top and bottom of the sample were in contact with filter papers and
175 ceramic porous discs connected to outlets. The cell was placed in a rigid frame that guaranteed the
176 constant volume of the sample by hindering the displacement of the piston. An external LVDT
177 measured the potential axial displacements, whereas a 10-t load cell in the upper part of the frame
178 measured the force developed by the specimen with a precision of 0.2% (equivalent to ± 1 kPa for an
179 axial pressure of 0.5 MPa). This cell was used in previous investigations using pellets or compacted
180 powder separately (Imbert and Villar 2006, Villar 2012).



181

182 **Fig. 1. Schematic representation of the oedometer cell**

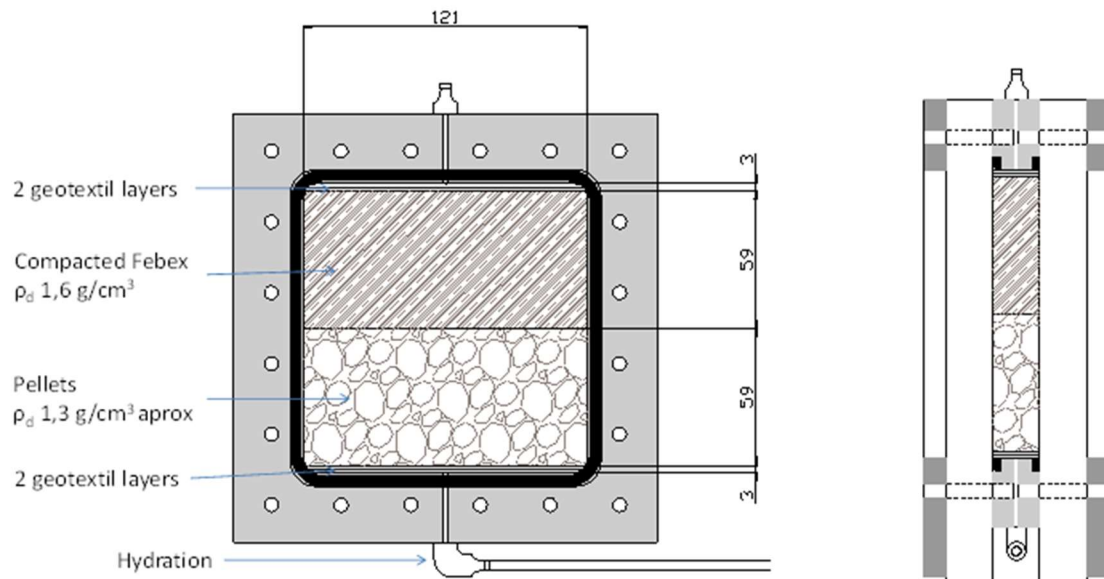
183 The lower half of the cell was filled with bentonite pellets with an average dry density close to 1.30
 184 g/cm^3 and the upper part by a bentonite block of nominal dry density 1.60 g/cm^3 , except in test
 185 MGR27, in which the position of block and pellets was inverted. The bentonite was directly
 186 compacted inside the cell with its hygroscopic water content. The pellets were poured on this block
 187 and carefully shaken as necessary to get the target density (Fig. SM1 in Supplementary Material,
 188 available online). Then the cell was overturned and mounted in the oedometric frame. The water
 189 intake took place through the bottom surface, either under a low injection pressure (a 1.5-m water
 190 column, 15 kPa) or under a constant low flow ($0.05 \text{ cm}^3/\text{h}$). In the first case the water intake was
 191 measured with an automatic volume change apparatus and in the second case with a
 192 pressure/volume controller. During hydration the top outlet remained open to atmosphere and the
 193 pressure exerted by the material, the sample deformation and the water intake were measured and
 194 automatically recorded. A summary of the tests performed and of their characteristics is given in Tab.
 195 2 and Tab. 3.

| Test | Hydration | Duration (days) | Observations | T (°C) |
|-------------|--|------------------------|---------------------------|---------------|
| MGR21 | Constant pressure: 15 kPa | 34 | Including pellets >9.5 mm | 23.1±0.6 |
| MGR22 | Constant flow: 0.05 cm ³ /h | 266 | Including pellets >9.5 mm | 22.5±1.3 |
| MGR23 | Constant pressure: 15 kPa | 210 | Pellets dried | 22.6±1.5 |
| MGR24 | Constant pressure: 15 kPa | 14 | Pellets dried | 22.5±0.6 |
| MGR25 | Constant pressure: 15 kPa | 76 | Pellets dried | 22.7±1.1 |
| MGR26 | Constant flow: 0.05 cm ³ /h | 132 | Pellets dried | 23.6±1.2 |
| MGR27 | Constant pressure: 15 kPa | 278 | Pellets dried | 23.0±1.2 |

197

198 **2.3 Tests in transparent cell**

199 The transparent cell or window cell (CW) is a custom-built square cell consisting of two transparent
200 methacrylate faces screwed to a steel frame (Fig. 2). The inner dimensions of the steel frame are
201 121x118x20 mm. A square block of the same dimensions was compacted in a bespoke mould and
202 half sectioned. One of the halves was placed in the cell and the rest of the cell was homogeneously
203 filled with the pellets while the cell was horizontally laid. Photographs of the mounting process are
204 shown in Fig. SM2. During assembly the fine fractions moved towards the bottom. The side of the cell
205 which was at the bottom during assembly was called B-face. Hence, the two faces of the cells, A and
206 B, presented different appearance (Fig. SM3).



207

208 **Fig. 2. Schematic front and lateral views of the transparent cell (CW1 with pellets at the bottom, as shown in the Figure,**
 209 **and CW2 with pellets on top)**

210 Two geotextile layers were placed at the upper and bottom sides of the cell. Hydration took place
 211 through the bottom with a 30-cm (3 kPa) water column. In test CW1 the pellets were placed at the
 212 bottom, and inversely, in test CW2 the block was at the bottom and consequently was the first part
 213 to be hydrated. Photographs of both sides were periodically taken.

214 The tests were performed at room temperature ($23\pm 1^\circ\text{C}$). Test CW1 lasted 379 days and test CW2
 215 lasted 420 days.

216 **2.4 Postmortem analyses**

217 At the end of the tests the samples were extracted from the cell (by pushing with a piston in the case
 218 of cell MGR), measured, weighed, and cut in regular horizontal sections. Each section was
 219 subsampled to determine water content, dry density and the pore size distribution. The cylindrical
 220 blocks from MGR tests were sliced in 6 horizontal levels (3 for pellets and 3 for block). The CW

221 samples were cut into 15 parts (5 rows and 3 columns). The subsamples were numbered from top to
222 bottom, i.e. sample #1 was the one farther away from the hydration surface.

223 The gravimetric water content (w) is defined as the ratio between the mass of water and the mass of
224 dry solid expressed as a percentage. The mass of water was determined as the difference between
225 the mass of the sample and its mass after oven drying at 110°C for 48 hours. Dry density (ρ_d) is
226 defined as the ratio between the mass of the dry sample and the volume occupied by it prior to
227 drying. The volume of the specimens was determined by immersing them in a recipient containing
228 mercury and by weighing the mercury displaced, considering a density of mercury of 13.6 g/cm³.

229 The pore size distribution of subsamples was determined by mercury intrusion porosimetry (MIP).
230 The samples were put in the ice condenser of a Telstar LioQuest equipment at -30°C for 3 hours.
231 Subsequently, they were lyophilised for 22 hours at a temperature of -50°C under a vacuum of 0.2
232 mbar, so that to sublimate the water in the pores. Thereafter, they were heated at 25-30°C for 3
233 hours. These samples were kept in a desiccator until the MIP analysis. The porosimeter used was a
234 Micromeritics AutoPore Series IV 9500, which allowed the exploration of pore diameters between
235 0.007 and 600 μm . Prior to mercury injection the sample was outgassed by applying a vacuum of 50
236 $\mu\text{m-Hg}$. Afterwards the mercury injection pressure was increased from 2.7 kPa to 220 MPa in 109
237 steps. To determine the extrusion branch of the curve, the pressure was released in 56 steps down to
238 a pressure of 68.6 kPa. A contact angle of mercury of 139° both on advancing and of receding on the
239 clay surface was considered.

240 The (001) reflection or basal reflection gives the distance along the crystallographic c -axis between
241 clay lamellae and for a given clay mineral depends on the exchangeable cations present in the
242 interlayer and their degree of hydration. To determine it, subsamples were preserved in paraffined
243 foil after dismantling of the cells and the X-ray diffraction profile of a plane surface of them was
244 registered at laboratory temperature after removing the foil and without any further treatment. An

245 anode of Cu (CuK α) radiation was used with a Philips model X'Pert-MPD diffractometer at 40 mA, 45
246 kV operating condition. The profiles were obtained with a 0.1-mm entrance slit and a scanning rate
247 of 0.025°2 θ /s. Data were collected between 2 and 10°2 θ . The goniometer settings were: automatic
248 divergence slit and diffracted beam slit 2 mm. In other samples, an anode of Cu (CuK α) radiation was
249 used with a Bruker D8 Advance diffractometer at 40 mA and 40 kV operating conditions. XRD
250 experimental profiles were obtained with a 1-mm entrance slit, 0.05°2 θ step size and a counting time
251 of 3 s per step. Data were collected between 2 and 30°2 θ . The divergence slit and diffracted beam
252 slit of the goniometer were fixed at 1 mm. In both cases the position of the diffraction peaks was
253 adjusted by using the quartz in the samples as an internal standard. The complete mathematical
254 description of the scan pattern was obtained by combination of a polynomial function that describes
255 the background and a profile function that fits the experimental reflections. The pseudo-Voigt profile
256 function was used to fit the diffraction peaks as well as to deconvolute overlapped reflections.

257 Additionally, in each CW test a cylindrical subsample was obtained by drilling across the block/pellet
258 interface to measure the gas breakthrough pressure as an indicator of the sealing quality of the
259 interface. This subsample was vertically crossed by the interface. The core diameter was fit to 3.8 cm
260 by using a cutting ring and knife. Filter paper and porous stones were placed on top and bottom of
261 the sample and it was laterally wrapped in double latex membranes. Vacuum grease was applied
262 between membranes in order to prevent the loss of gas. The wrapped sample was placed in a triaxial
263 cell which was filled with de-aired water and pressurized to ensure perfect adherence of the
264 membranes to the surface of the sample and avoid gas transport along it. The cell inlet at the upper
265 part of the sample was connected to a nitrogen gas cylinder applying the gas injection. The outlet of
266 the cell connected to the bottom of the sample was open to atmosphere, with a series of different
267 range gas mass flowmeters measuring the gas outflow. More experimental details about the
268 equipment and the equations used to compute permeability are given in Villar et al. (2018, 2021).
269 Gas was applied through face A (that of coarser granulometry, Fig. SM3). The particular test

270 procedure was adapted to the characteristics of the samples. In test CW1 the injection pressure was
271 increased until outflow occurred and in test CW2 the confining pressure was increased until flow
272 stopped.

273 **3 Results**

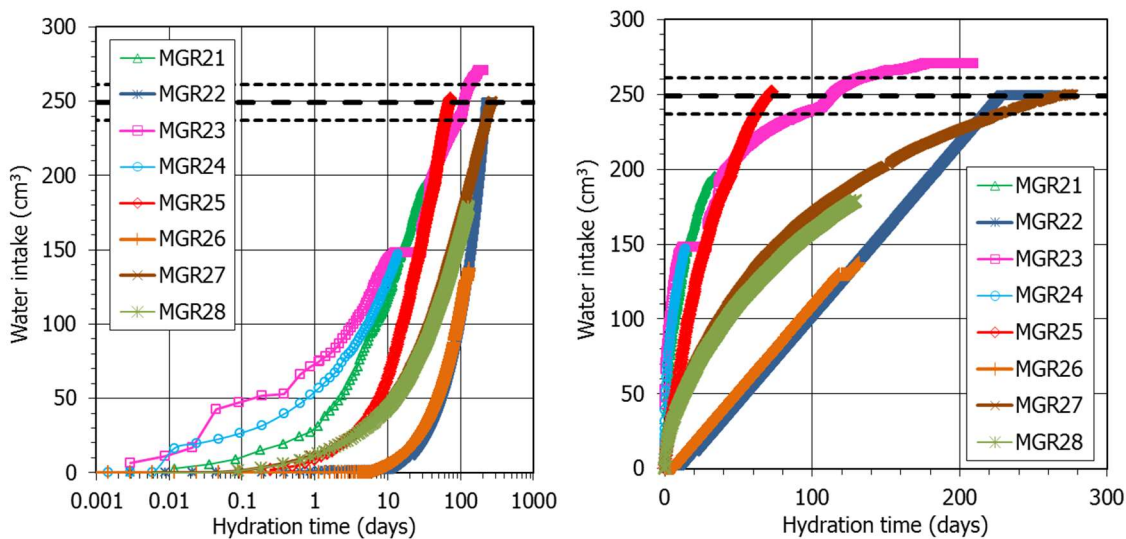
274 **3.1 Hydration process**

275 **3.1.1 Large-scale oedometer: online measurements**

276 Water intake, axial pressure and vertical deformation were continuously measured during hydration.
277 Vertical deformation was minimal, since the movement of the piston was blocked by the oedometer
278 framework. In fact the changes in overall dry density occurred as a result of the small vertical
279 deformation allowed were in all cases below 0.005 g/cm^3 . Fig. 3 and Fig. 4 show the evolution of
280 water intake and axial pressure for the seven tests. The tests were stopped and dismantled after
281 different periods of time to get the temporal evolution of the postmortem information detailed in
282 sections 3.2.1, 3.3.1 and 3.4. Tests MGR22 and MGR23 continued until a pressure plateau was
283 reached.

284 Fig. 3 also shows the water intake necessary to reach full saturation ($250 \pm 12 \text{ g}$), which was not the
285 same for all the tests because of the slight differences among them in initial dry density and water
286 content (Tab. 3). Some of the tests reached full saturation. There was a significantly different
287 behaviour between the tests performed under constant injection pressure (MGR21, MGR23, MGR24
288 and MGR25) and the tests performed under constant water inflow rate (MGR22 and MGR26). In the
289 constant-pressure tests the water intake was very quick and more than half of the water volume
290 necessary for full saturation was taken in about 20 days, which was probably caused by the high
291 permeability of the pellets part. In contrast, the water intake was much slower in the two tests in

292 which constant flow was prescribed, and it took more than 100 days to reach overall degrees of
 293 saturation close to 50%. The water intake rate in test MGR27, in which hydration took place through
 294 the block part of the column (which was placed at the bottom), was initially intermediate between
 295 that of tests performed under constant pressure and those performed under constant inflow.
 296 However, it showed the slowest water intake rate in the long run, attesting the lower permeability of
 297 the higher density block. Some of the differences among the tests, particular concerning the initial
 298 water intake, were likely caused by experimental artefacts. In test MGR23 there was a short period
 299 (~14 days) during which no water was supplied to the cell because air entered the hydration line. As
 300 shown in Fig. 4, this did not affect the swelling pressure evolution.



301
 302 **Fig. 3. Water intake evolution in the large-scale oedometer tests in log and linear temporal scales (constant flow was**
 303 **prescribed in tests MGR22 and MGR26). The thick horizontal lines indicate the water intake necessary to reach full**
 304 **saturation (average and standard deviation). In tests MGR22 and MGR26 the water intake includes partly the intake of**
 305 **the bottom porous stone (6-14 cm³)**

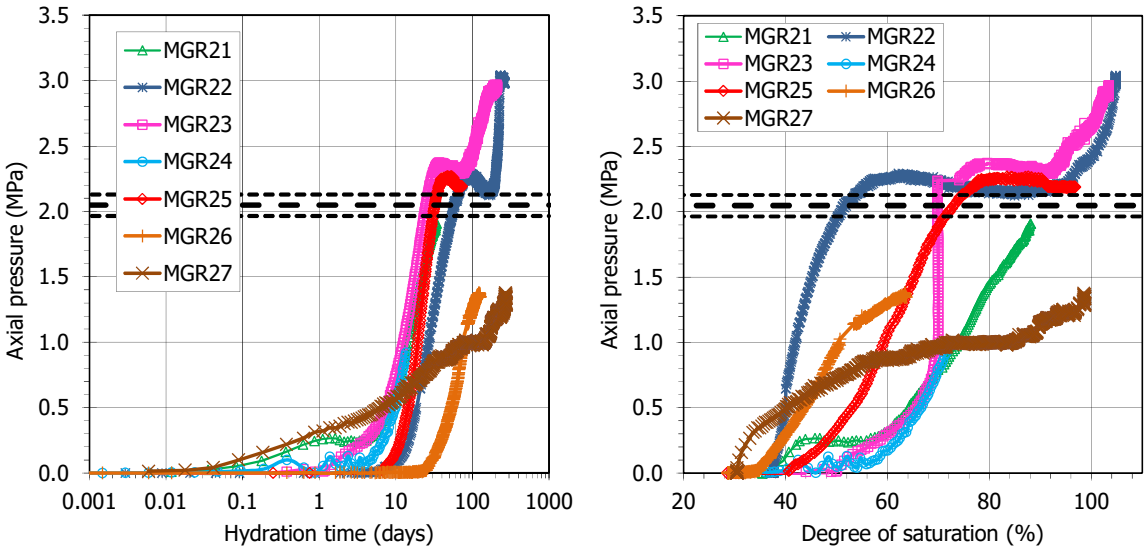
306 Fig. 4 shows the axial pressure development over time and as a function of the overall degree of
 307 saturation (Fig. SM4 shows the evolution of axial pressure over time in a linear temporal scale). The
 308 degree of saturation shown in Fig. 4 is an overall value for the two-component samples but, at any

309 given time, the actual degrees of saturation at different points along the sample height were very
310 different, as the postmortem determinations presented in section 3.2.1 showed.

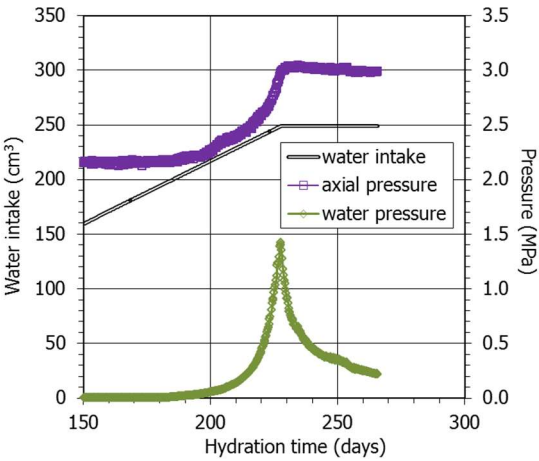
311 In terms of temporal evolution, the axial pressure build up was generally steep at the beginning. In
312 the longer tests, after the initial peak there was a smooth decrease in axial pressure that eventually
313 recovered and continued increasing after final stabilisation. The initial pressure peak occurred for
314 overall degrees of saturation close to 80% in tests MGR23 and MGR25. In test MGR23 the period of
315 time during which the axial pressure significantly increased with no change in the overall degree of
316 saturation corresponds to the ~14 days period during which inadvertently no water was supplied to
317 the cell. The fact that pressure continued to build up would indicate that water redistribution inside
318 the bentonite can cause pressure increase. In contrast, in test MGR22, performed under controlled
319 flow conditions, axial pressure peaked for an overall degree of saturation of only ~60%. This would
320 mean that slow saturation was more efficient, in the sense that it allowed a better water
321 redistribution inside the microstructure.

322 In the long test MGR23, after the sharp initial increase (the peak was reached at 30-40 days), there
323 was an intermediate stage of slight pressure decrease, and when the average degree of saturation
324 was ~90% the axial pressure steadily increased again until full saturation was reached, with a stable
325 pressure value of 3 MPa. Test MGR22 also went on until full saturation was reached. Since in this test
326 the inflow was very low and controlled, the pressure development kinetics was very different to the
327 other tests. Axial pressure started to develop slightly later than in the other tests (after 10 days), and
328 when the overall degree of saturation was much lower than in the other tests (37%). The first peak
329 was reached after 80 days and the intermediate stage lasted until 200 days had elapsed. During this
330 time the overall degree of saturation increased from 58 to 96%. In the final stage, the water injection
331 pressure started to increase because the P/V controller was not able to keep a constant low injection
332 flow into a quasi-saturated sample without increasing the injection pressure. As a result, there was a

333 new steep increase in axial pressure until the final value of 3 MPa. When the water injection pressure
 334 had increased to 1.5 MPa, water injection was stopped and the pressure was allowed to dissipate for
 335 38 days. This explains the odd final shape of the curves for test MGR22. During this period of water
 336 injection pressure decline, the axial pressure did not change (Fig. 5).



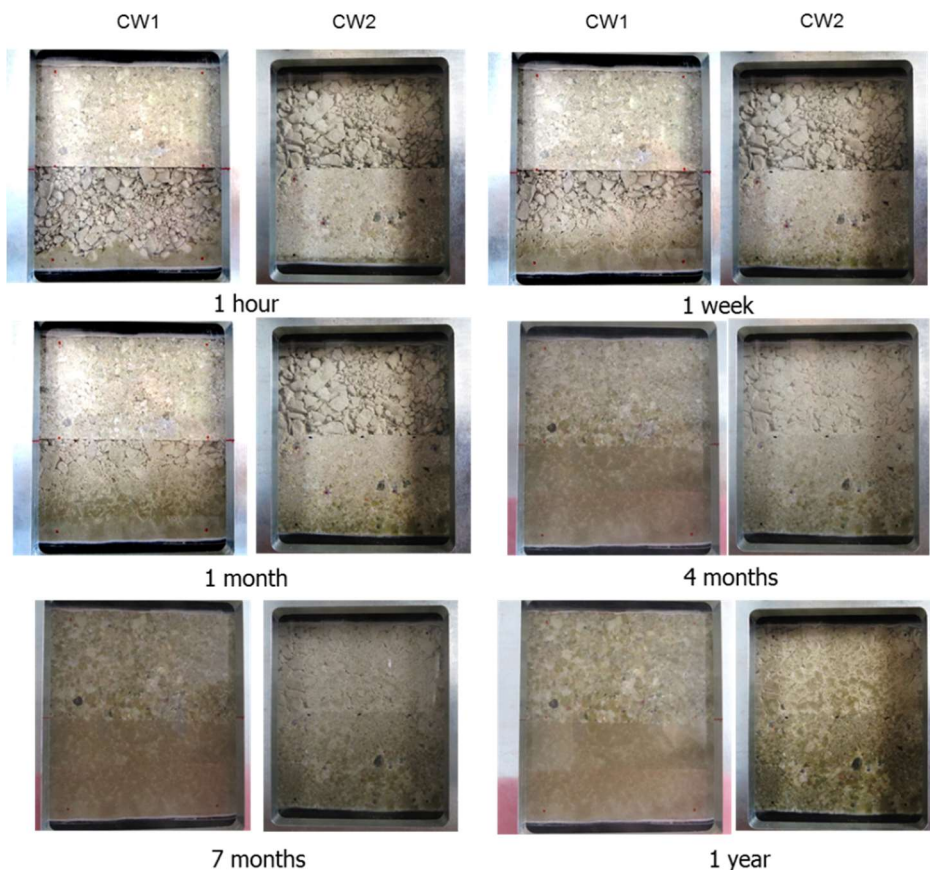
337
 338 **Fig. 4. Axial pressure evolution over time (left) and as a function of the overall degree of saturation (right) in the large-**
 339 **scale oedometer tests (constant flow was prescribed in tests MGR22 and MGR26). The thick horizontal lines indicate the**
 340 **expected swelling pressure according to Eq. 3 (average and standard deviation)**



341
 342 **Fig. 5. Final stage of test MGR22**

343 **3.1.2 Transparent cell: visual observations**

344 Cells CW1 and CW2 were photographed on both sides (A and B faces) periodically during hydration.
345 Fig. 6 shows a comparison of the appearance of face A of the two tests at the same testing times
346 (and Fig. SM5 for face B). Variations in the coloration of the grains, changes in texture and shape, and
347 displacement of the block-pellets interface were observed. As the pellets were hydrated, the grains
348 increased in size, without displacement, and the whole of them lose sharpness. The appearance of
349 the saturated pellets was gel-like. The evolution of hydration was slower in face B, where fine
350 particles predominated. The reason could be the absence of large voids where water could quickly
351 and easily penetrate. A downwards movement of the pellets/block interface in cell CW1 was
352 observed, whereas this interface moved upwards in cell CW2.



353

354 **Fig. 6. Comparison, in face A, of the evolution of the hydration fronts in both cells (CW1: first and third column, and CW2:**
355 **second and fourth column) for six different moments**

356 **3.2 Final physical state**

357 **3.2.1 Large-scale oedometer**

358 The tests were dismantled after different running times. The final appearance of the samples once
359 extracted from the cell is shown in Fig. 7 for the tests performed hydrating from the pellets half
360 under constant injection pressure and in Fig. 8 for the rest of tests. The sample from the shorter test
361 (MGR24) showed a quite saturated bottom in which the pellets could not be told apart, but the
362 upper part of the pellets half still showed open voids. The two halves of this sample (pellets and
363 block) could easily be detached. In the other cases the two halves were sealed and had to be
364 separated with a knife. Already after 76 days the pellets half looked homogeneous. In contrast, in the
365 tests performed under constant inflow rate, after 132 days (test MGR26) some pellets could still be
366 told apart. In test MGR27 (saturated through the block), although the block looked saturated, the
367 pellets upper part still presented voids from the initial fabric.



368 MGR24: 14 days

MGR21: 34 days

MGR25: 76 days

MGR23: 210 days

369 **Fig. 7. Appearance of the MGR samples at the end of the tests performed under constant water injection pressure**



MGR26: 132 days

MGR22: 266 days

MGR27: 278 days

370

371 **Fig. 8. Appearance of the MGR samples at the end of the tests performed under constant water inflow rate (MGR22,**
372 **MGR26) and with saturation through the block (MGR27)**

373 Once extracted the blocks were weighed, measured and horizontally sectioned to determine the
374 longitudinal changes in water content, dry density and pore size distribution. Tab. 3 shows a
375 summary of the final characteristics of the samples, along with the initial values. The original height
376 of the halves changed during the tests: the height of the bottom, pellets half decreased whereas the
377 height of the upper, block half increased, indicating the increase in the overall dry density of the
378 pellets and decrease in the dry density of the block. These changes are illustrated in Fig. 9 and were
379 confirmed by the postmortem determination of dry density in the six horizontal sections. The water
380 content of the bottom part (pellets) increased very quickly, but over time tended to decrease. In
381 contrast, the dry density of the pellets half increased in a more continuous way. The behaviour of
382 test MGR26 performed under constant flow (lasting 132 days) did not follow the overall trend, since
383 the increase in water content was moderate and similar for both halves, attesting the more
384 homogeneous water redistribution allowed by slow hydration. The two longest tests, which were
385 performed under constant water inflow (MGR22) or with the block at the bottom (MGR27) should be
386 separately considered. When hydration took place through the block, the final water content and dry
387 density of both halves were more homogeneous.

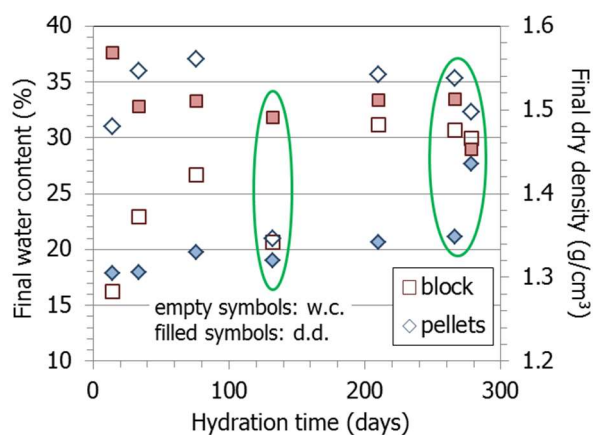
Tab. 3. Initial and final characteristics of MGR tests

| | Initial | | | Final | | | | |
|--------------------|-----------------|----------|-------------------------------|-----------|---------|-------------------------------|----------|-----------|
| | w (%) | h (cm) | ρ_d (g/cm ³) | S_r (%) | w (%) | ρ_d (g/cm ³) | h (cm) | S_r (%) |
| Test | MGR21, 34 days | | | | | | | |
| Pellets | 9.5 | 4.97 | 1.26 | 23 | 35.9 | 1.31 | 4.80 | 91 |
| Block | 13.3 | 5.01 | 1.60 | 52 | 22.9 | 1.50 | 5.33 | 78 |
| Total ^a | 11.6 | 9.98 | 1.43 | 35 | 29.0 | 1.43 | 10.00 | 88 |
| Test | MGR22, 266 days | | | | | | | |
| Pellets | 9.9 | 5.04 | 1.28 | 24 | 35.3 | 1.35 | 4.79 | 95 |
| Block | 13.6 | 4.94 | 1.61 | 55 | 30.7 | 1.51 | 5.27 | 106 |
| Total ^a | 11.9 | 9.98 | 1.45 | 37 | 32.7 | 1.44 | 10.01 | 101 |
| Test | MGR23, 210 days | | | | | | | |
| Pellets | 3.5 | 5.00 | 1.30 | 9 | 35.7 | 1.34 | 4.84 | 95 |
| Block | 14.2 | 4.98 | 1.60 | 56 | 31.1 | 1.51 | 5.29 | 107 |
| Total ^a | 9.4 | 9.98 | 1.45 | 29 | 33.2 | 1.45 | 10.01 | 103 |
| Test | MGR24, 14 days | | | | | | | |
| Pellets | 5.7 | 5.02 | 1.28 | 14 | 31.0 | 1.30 | 4.93 | 78 |
| Block | 13.7 | 4.97 | 1.62 | 55 | 16.2 | 1.57 | 5.13 | 61 |
| Total ^a | 10.1 | 9.99 | 1.45 | 32 | 23.0 | 1.45 | 10.00 | 72 |
| Test | MGR25, 76 days | | | | | | | |
| Pellets | 3.2 | 4.99 | 1.30 | 8 | 37.0 | 1.33 | 4.88 | 97 |
| Block | 14.1 | 5.00 | 1.59 | 54 | 26.7 | 1.51 | 5.24 | 92 |
| Total ^a | 9.2 | 9.99 | 1.44 | 29 | 31.4 | 1.44 | 10.02 | 97 |
| Test | MGR26, 132 days | | | | | | | |
| Pellets | 3.5 | 5.01 | 1.30 | 9 | 21.0 | 1.32 | 4.92 | 54 |
| Block | 13.9 | 4.99 | 1.60 | 55 | 20.6 | 1.49 | 5.35 | 69 |

| | Initial | | | Final | | | | |
|--------------------|-----------------|----------|-------------------------------|-----------|---------|-------------------------------|----------|-----------|
| | w (%) | h (cm) | ρ_d (g/cm ³) | S_r (%) | w (%) | ρ_d (g/cm ³) | h (cm) | S_r (%) |
| Total ^a | 9.2 | 10.00 | 1.45 | 29 | 20.8 | 1.44 | 10.07 | 64 |
| Test | MGR27, 278 days | | | | | | | |
| Pellets | 3.0 | 5.00 | 1.31 | 8 | 32.3 | 1.43 | 4.55 | 99 |
| Block | 15.3 | 5.00 | 1.59 | 59 | 30.0 | 1.45 | 5.47 | 94 |
| Total ^a | 9.8 | 10.00 | 1.45 | 30 | 31.7 | 1.45 | 10.02 | 99 |

389 ^a the initial values are the averages of block and pellets, the final values correspond to online measurements (except in test MGR22)

390



391

392 **Fig. 9: Final average water content and dry density of the block and pellet halves of the samples (the values circled**

393 **correspond to tests performed under constant inflow rate (MGR22, MGR26) or with the block at the bottom (MGR27)**

394 The water content and dry density values measured in subsamples are plotted in Fig. 10 as a function

395 of the distance to the hydration surface. The initial values are indicated with thick horizontal lines.

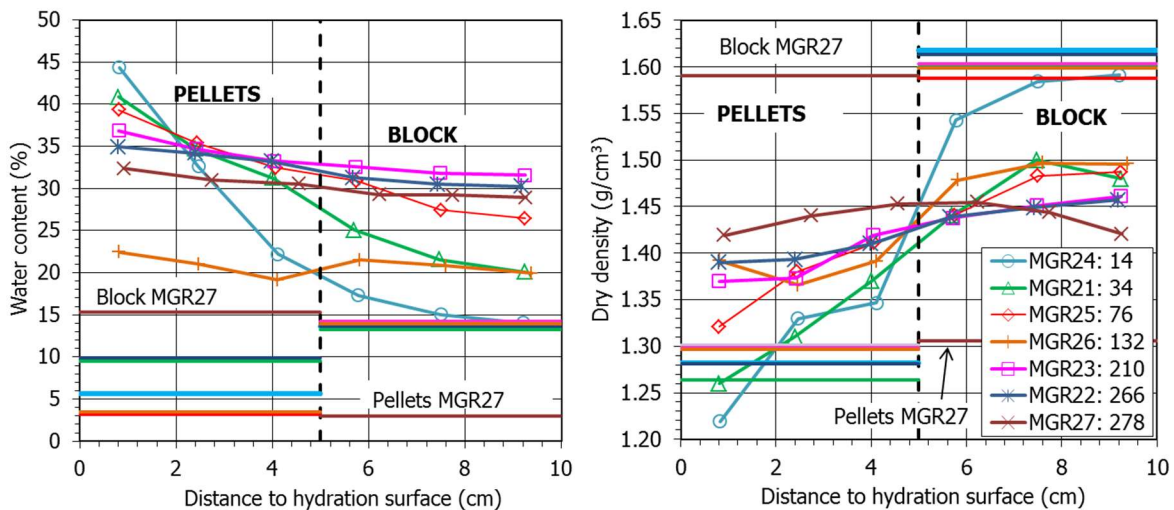
396 The differences in the initial water content of the pellets were caused because in tests MGR23 to

397 MGR27, prior to mounting, the pellets were dried to the values they had after they were

398 manufactured (Tab. 2). During the tests the water content and degree of saturation decreased from

399 the hydration surface (sample bottom) upwards whereas the dry density increased. These gradients

400 attenuated over time, hence they were smoother as the test duration was longer. The pellets/block
 401 interface did not seem to have any effect on the continuous gradients. The final dry density and
 402 water content values were similar in tests MGR22 and MGR23, despite the different hydration
 403 conditions (constant flow or pressure). Although the bentonite was finally fully saturated, the dry
 404 density and water content along the samples did not completely equalise. In contrast, test MGR26,
 405 which was far from full saturation, showed a quite homogeneous water content distribution,
 406 whereas the difference between the dry density of pellets and block was still significant.

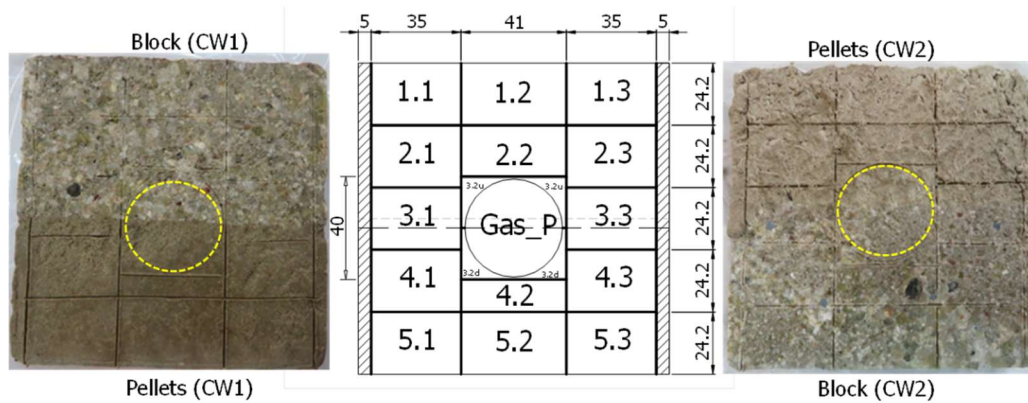


407
 408 **Fig. 10.** Final water content and dry density along the samples of MGR tests. The duration of the tests is given in days in
 409 the legend. The thick horizontal lines mark the initial values

410 3.2.2 Transparent cell

411 Cell CW1, saturated through the pellets, was dismantled after 379 days and cell CW2, saturated
 412 through the block, after 420 days of hydration. A detailed characterisation of the final state of the
 413 bentonite was carried out in subsamples taken according to the schema shown in Fig. 11. It was not
 414 possible to distinctly separate the block and pellet parts. Tab. 4 summarises the initial and final
 415 characteristics of the tests. For the global values, the initial and final dimensions and weight of the
 416 pellets/block assemblage were considered. Because bentonite swelling caused the compression of

417 the geotextiles placed on top and bottom of the cell (Fig. 2), the total height of the sample increased
 418 and hence there was an overall decrease in dry density. Cell CW1 had reached full saturation, but not
 419 cell CW2, despite its longer duration. The values shown in the Table for the block and pellets parts
 420 are the average of the determinations in subsamples. These may be affected by trimming and slight
 421 drying during manipulation.



422

423 **Fig. 11. Final subsampling of tests CW and location of samples for gas permeability (circle)**

424 **Tab. 4. Initial and final characteristics of tests CW1 and CW2**

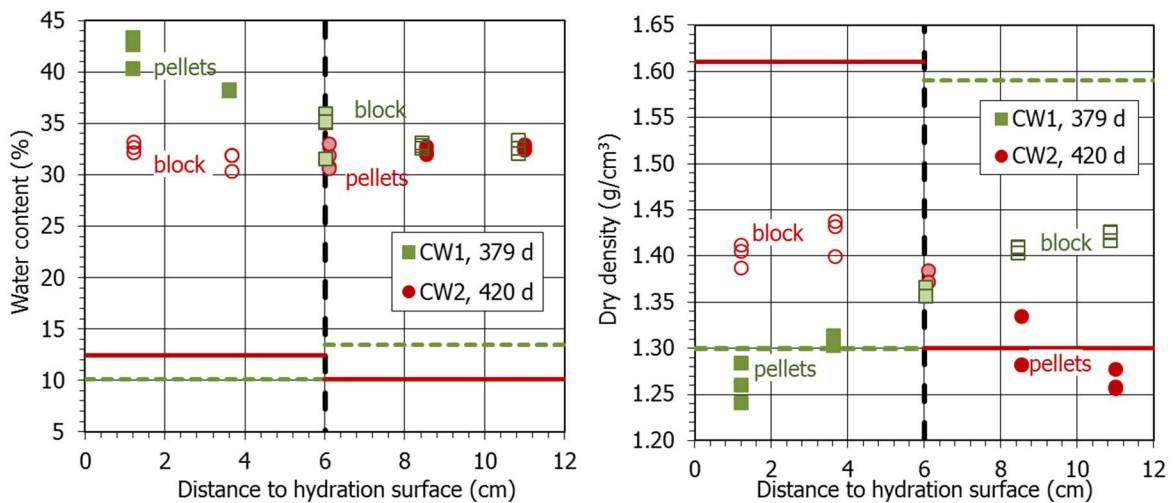
| Test | Initial | | | | Final | | | |
|------------------------|---------|-------|-------------------------------|-----------|--------|-------|-------------------------------|-----------|
| | h (cm) | w (%) | ρ_d (g/cm ³) | S_r (%) | h (cm) | w (%) | ρ_d (g/cm ³) | S_r (%) |
| Pellets ^a | 5.75 | 10.1 | 1.30 | 25 | 5.69 | 40.5 | 1.28 | 99 |
| CW1 Block ^a | 6.03 | 14.0 | 1.59 | 54 | 6.37 | 32.8 | 1.47 | 105 |
| Total ^b | 11.79 | 11.9 | 1.45 | 37 | 12.06 | 35.9 | 1.38 | 102 |
| Pellets ^a | 5.60 | 10.1 | 1.30 | 25 | 5.58 | 32.4 | 1.31 | 82 |
| CW2 Block ^a | 5.98 | 12.4 | 1.61 | 50 | 6.64 | 32.1 | 1.45 | 101 |
| Total ^b | 11.58 | 11.2 | 1.46 | 36 | 12.22 | 32.1 | 1.39 | 92 |

425 ^a final dry density and degree of saturation affected by subsampling and trimming, ^b final values affected by compression of
 426 geotextile during test

427

428 Fig. 12 shows the final water content and dry density determined in the subsamples of the two tests,
429 along with the initial values. Hydration resulted in an overall water content increase both in the
430 pellets and the block parts, considerably higher for the pellets part of test CW1. As a result of the
431 water content increase, the bentonite swelled and the dry density of the assemblage decreased
432 because of the slight deformation allowed by the geotextile compression (the overall dry density of
433 cell CW decreased from 1.45 to 1.38 g/cm³ and that of cell CW2 from 1.46 to 1.39 g/cm³). In both
434 tests the swelling was higher in the block part, whose dry density significantly decreased. Despite the
435 fact that the sample CW1 was fully saturated at the end of the test (Tab. 4), there were still clear
436 water content and dry density gradients, with higher water contents and lower dry densities in the
437 pellets part, which was earlier saturated. In contrast, cell CW2, which was not completely saturated,
438 showed homogeneous water content but still considerably higher dry densities and degrees of
439 saturation in the block part. In fact, the average degree of saturation of the pellets part was only of
440 82%. The interface between pellets and block did not seem to play any role in the general trend of
441 these variables.

442 However, a small border effect was observed at the bottom of the cells: the water content of the
443 subsamples close to the border (5.1 and 5.3 in Fig. 11) was higher than that of the middle subsample
444 (5.2), whereas the dry density was lower, especially in cell CW1. The cell border effect persisted,
445 although weakened, until the upper part (e.g. samples 1.1 and 1.3 had slightly higher water content
446 and lower dry density than sample 1.2).



447

448 **Fig. 12. Final water content and dry density along the samples of CW tests. The duration of the tests is given in days. The**
 449 **thick horizontal lines mark the initial values (discontinuous lines for CW1)**

450 3.3 Pore size distribution

451 The pore size distribution of the samples was determined by mercury intrusion porosimetry (MIP). In
 452 some subsamples duplicates were tested. In the sections below, the intrusion curves obtained in
 453 some of the samples are shown. In all of them the usual two pore families of compacted FEBEX
 454 bentonite corresponding approximately to pores larger and smaller than 200 nm could be told apart.
 455 This limit is not the same as that between macropores and mesopores, which according to the
 456 classification of Sing et al. (1985) would be at 50 nm. There is also discussion on the criteria that can
 457 be followed to select this delimiting value (Yuan et al. 2020). The ‘valley’ criterion was chosen in this
 458 work, consisting of using the lowest point of the valley between the two peaks of a bimodal
 459 distribution. In several THM models, this pore size represents the limit separating inter-aggregate
 460 from intra-aggregate pores, the latter not affected by density changes (e.g. Lloret et al. 2003,
 461 Sánchez et al. 2005, Mašín 2013).

462 The mercury intrusion method allows access to be gained only to part of the macroporosity (pores of
 463 diameter smaller than ~550 μm) and to part of the mesopores (those of diameters larger than 7 nm),

464 since mercury does not intrude the microporosity (pores of a size of less than 2 nm, according to the
465 same classification mentioned above). Actually, the percentage of pores intruded by mercury in the
466 samples analysed in this work was between 30 and 76%. Considering that most of the non-intruded
467 porosity corresponds to the pores of a size smaller than the limit of the apparatus (7 nm), an
468 estimation of the percentage of pores actually intruded can be made by comparing the actual void
469 ratio of the samples (e , computed from their dry density and density of solid particles) and the
470 apparent void ratio calculated from mercury intrusion (e^*). There is uncertainty in this approach,
471 since it is possible that pores larger than 7 nm were not intruded because of the bottleneck effect:
472 the pores connected to the external surface by narrow openings will not be intruded until sufficient
473 pressure is applied to intrude the entryways. All of the volume of such pores will be allocated to the
474 threshold radius class of the most restricted part of the entryway, which will result in an
475 overestimation of the smaller pore sizes volume. Likewise, although in compacted clay materials
476 pores larger than those that can be quantified by MIP are not expected, pores of this size could be
477 present in some of the driest pellets samples.

478 The intrusion curves of the subsamples are presented below along with the curves for FEBEX samples
479 of the same characteristics as the initial conditions used in the cells. For the block part, the curve
480 corresponding to a sample compacted at dry density 1.59 g/cm^3 with a water content of 14% was
481 used as representative of the initial state. For the pellets, mixtures of pellets having approximately a
482 Fuller's curve grain size distribution, with a resulting dry density of 1.29 g/cm^3 and water contents of
483 10 and 3% were used. The initial pellets curves showed a predominant pore size around $300 \mu\text{m}$.
484 Despite the low density of the pellets mixtures, the percentage of non-intruded porosity in them was
485 very high ($\sim 70\%$). In this case not all the non-intruded porosity can be ascribed to pores smaller than
486 7 nm, because in the dry, low-density pellets mixture large pores are also to be expected. Hence, an
487 estimation of the volume of pores larger than $550 \mu\text{m}$ has been made following this approach:

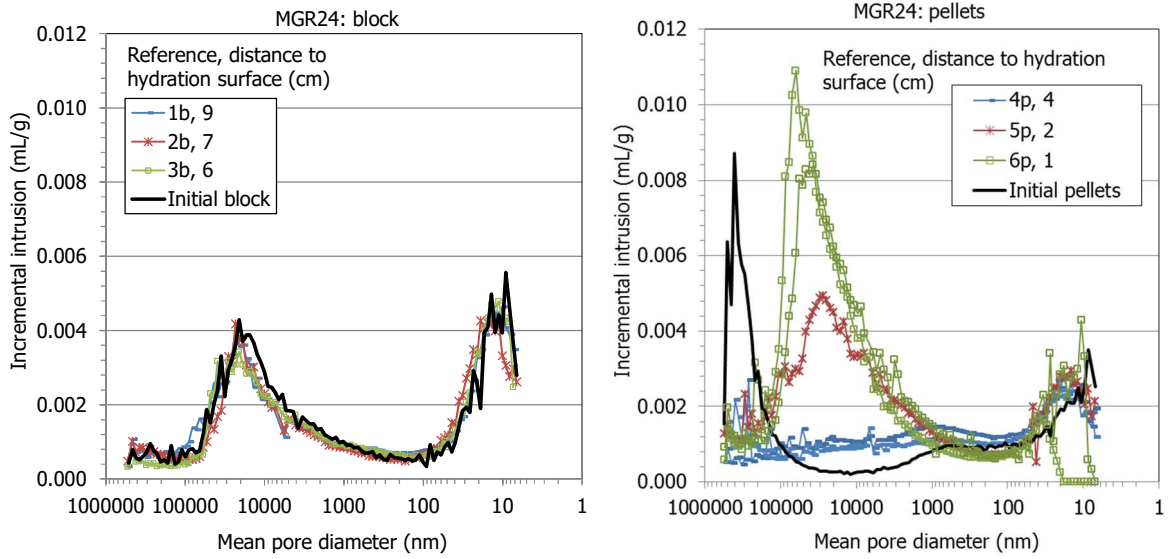
488 At the beginning of a MIP test the calibrated sample holder is filled with mercury under a low
489 injection pressure. Considering the sample mass and the volumes of the sample holder and of
490 mercury intruded, the dry density of the sample is computed by the equipment software. This initial
491 mercury injection is considered by the equipment as the zero value for the rest of the MIP test, which
492 actually starts when injection pressure is increased above this value. Thus, all the large porosity filled
493 during this initial step is disregarded. The comparison between the dry density determined by the
494 equipment at this step and the actual dry density of the sample allows computing the volume of
495 pores larger than 550 μm : when the sample contains a significant volume of large pores, the dry
496 density determined by the porosimeter is considerably higher than the actual dry density of the
497 sample, whereas if there are not large pores the two values tend to be similar. Hence, in the dry
498 pellets samples this difference was quite large, whereas in the saturated and high-density samples
499 the differences found were not significant. This correction was done to the initial GBM and to those
500 samples whose visual inspection clearly showed that contained large pores, namely samples MGR24-
501 4, MGR24-5, MGR21-4 (Fig. 7) and all the pellets samples from tests MGR26 (Fig. 8) and CW2. The
502 subsamples were numbered from top to bottom, i.e. sample #1 was the one farther away from the
503 hydration surface.

504 Taking all the above into account, the void ratio corresponding to pores larger and smaller than 200
505 nm (e_M and e_m , macro and micro, respectively) was recalculated, assuming that the non-intruded
506 porosity corresponded to pores smaller than the equipment injection capacity and, in some pellets
507 samples, also to pores larger than 550 μm .

508 **3.3.1 Large-scale oedometer test**

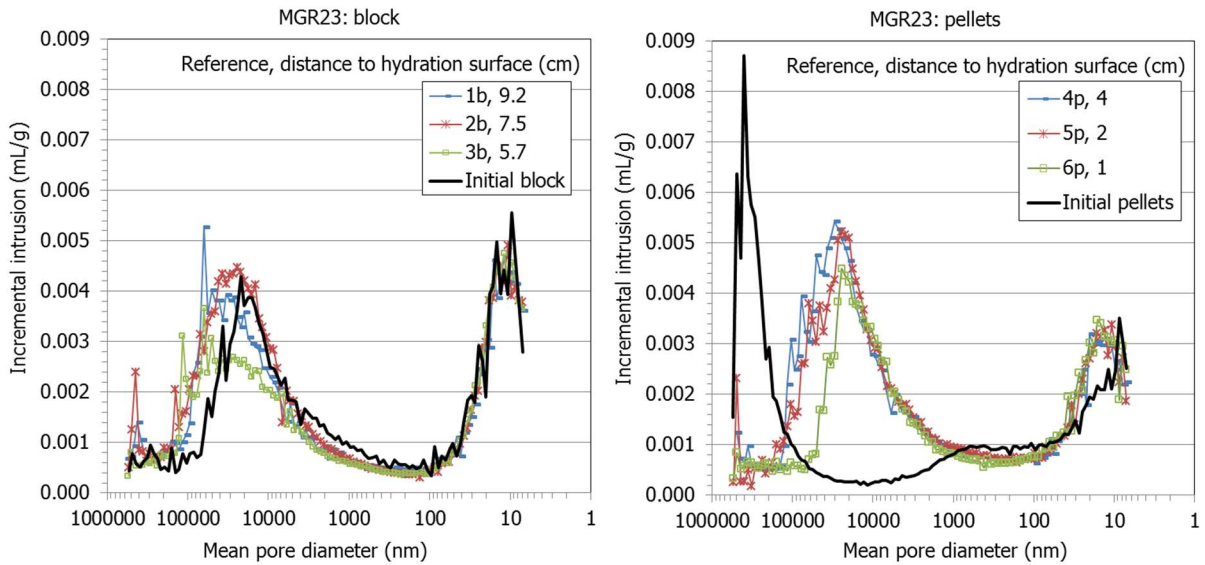
509 As an example, Fig. 13 and Fig. 14 show the incremental curves of mercury intrusion for the
510 subsamples of the tests lasting 14 (MGR24) and 210 days (MGR23). In the shorter test (Fig. 13) the
511 pore size distribution of the subsamples taken from the block half was similar to that of the initial

512 block. Indeed, no relevant changes in the dry density and water content of the block samples took
513 place during the oedometer test (only noticeable for the sample closest to the interface, 3b),
514 because it was too short. This similarity proves the reliability of the technique. In contrast, the pore
515 size distribution of the pellet half significantly changed. The size of pores larger than 200 nm and
516 their volume decreased with respect to the initial pellets mixture. A similar pattern was found in test
517 MGR21 (34 days). Overall, for the pellets subsamples of all the tests, the volume of pores larger than
518 200 nm significantly decreased, and the mean size of these macropores decreased from the initial
519 ~300 μm to values mostly between 10 and 100 μm . This can also be observed in Fig. 14 for the
520 subsamples from the pellets half of the longer test (MGR23). In contrast, the mean size of the pores
521 smaller than 200 nm increased with respect to the original values for all the pellets subsamples, as
522 well as for the block subsamples (Fig. 14 and Fig. SM6 for a summary of all the tests). Furthermore, in
523 the block subsamples the volume and size of the macropores also increased, except in the shorter,
524 less saturated tests. This overall increase in the pore volume of all the size ranges for the block
525 subsamples is related to the decrease in the global dry density of the block parts during the tests (Fig.
526 9).



527

528 Fig. 13. Pore size distribution expressed as incremental mercury intrusion of samples from test MGR24 (lasting 14 days),
 529 corresponding to the block (left) and pellets (right) halves. The curves for the initial materials (blocks and pellets) are
 530 included

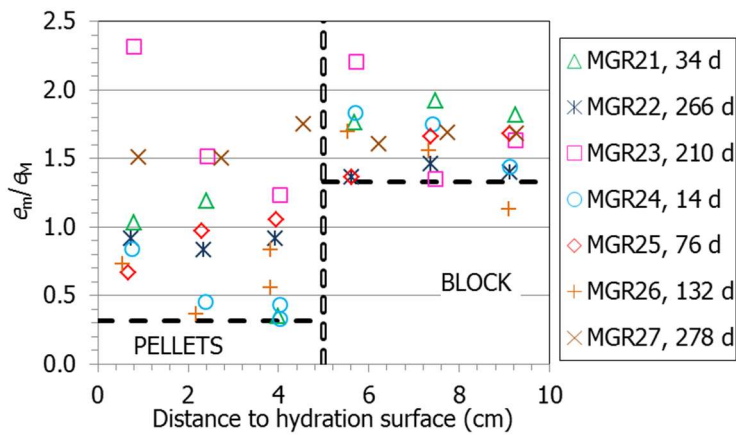


531

532 Fig. 14. Pore size distribution expressed as incremental mercury intrusion of samples from test MGR23 (lasting 210 days),
 533 corresponding to the block (left) and pellets (right) halves. The curves for the initial materials (blocks and pellets) are
 534 included

535 The void ratio corresponding to pores larger and smaller than 200 nm was recalculated as explained
 536 at the beginning of section 3.3. The ratio between the void ratio corresponding to pores smaller (e_m)

537 and larger (e_M) than 200 nm increased in all samples with respect to the reference values, which
 538 reflects the increase in the volume of micropores as a result of hydration (Fig. 15). This increase was
 539 much more significant for the pellets subsamples, except in the driest ones. In the block samples the
 540 largest proportion of void ratio corresponded to the pores of diameter smaller than 200 nm, and in
 541 fact for each test the largest e_m/e_M values tended to be in the block samples. The highest
 542 homogeneity in terms of e_m/e_M was reached in test MGR27, saturated through the block, which also
 543 had the most homogeneous dry density.

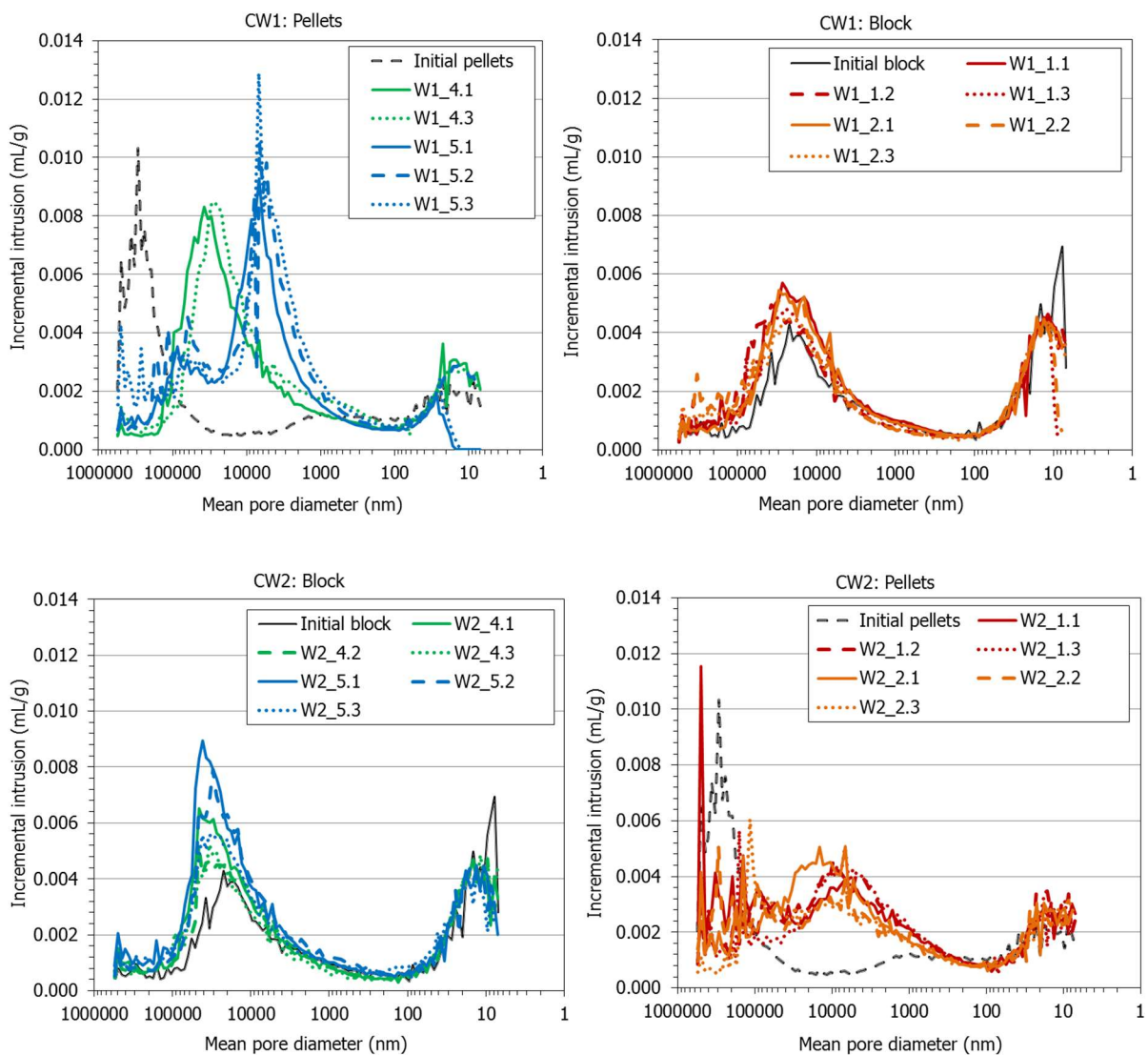


544
 545 **Fig. 15. Ratio between void ratio corresponding to pores smaller and larger than 200 nm (e_m and e_M) obtained by MIP in**
 546 **subsamples from the MGR tests (the thick horizontal lines indicate the initial conditions for all the tests except MGR27,**
 547 **in which the position of pellets and block was inverted)**

548 3.3.2 Transparent cell

549 Fig. 16 shows the incremental curves of mercury intrusion as a function of the mean pore diameter
 550 of the diameter size intervals corresponding to each pressure increase step. In both tests the
 551 macroporosity of the pellets shifted to smaller pore sizes, more as the water content was higher. In
 552 particular, for the pellets part in test CW1 the mean size of the macropores considerably decreased,
 553 from $\sim 300 \mu\text{m}$ to values between 6 and $40 \mu\text{m}$. However, in some cases, pores larger than $\sim 70 \mu\text{m}$
 554 remained, particularly in CW2, where the pellets part was not completely saturated. The pore size

555 distribution of the block parts did not change much as a result of hydration, particularly in test CW1.
 556 In the block part of test CW2 the size and volume of the macropores increased. All the samples had
 557 mean pore diameters for the pores smaller than 200 nm in a narrow range between 6 and 26 nm,
 558 and in test CW1 tended to decrease away from the hydration surface. In general the mean size of this
 559 pore family was higher than that for the initial block.

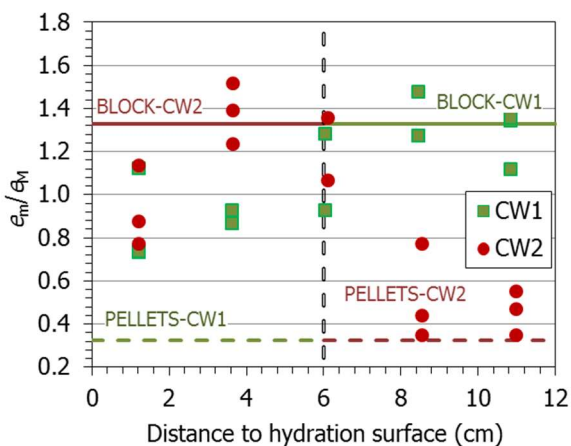


560

561

562 Fig. 16. Incremental mercury intrusion in tests CW1 and CW2 (the curves corresponding to the initial conditions are also
 563 included)

564 The ratio e_m/e_M obtained by MIP for the different subsamples is shown in Fig. 17 as a function of the
 565 distance to the hydration surface. For the pellets part in test CW1 the void ratio corresponding to
 566 pores larger than 200 nm considerably decreased, particularly away from the hydration surface. As a
 567 result, the e_m/e_M ratio increased in the same direction. In the pellets part of test CW2, the volume of
 568 large pores decreased only in some samples (except close to the pellets/block interface, where it
 569 significantly decreased), but the volume of pores smaller than 200 nm tended to increase, resulting
 570 in an increase of the e_m/e_M ratio in this area. In the block samples of both tests the largest proportion
 571 of void ratio corresponded to the pores of diameter smaller than 200 nm ($e_m/e_M > 1$), but both e_m and
 572 e_M increased with respect to the initial values, reflecting the overall decrease in dry density allowed
 573 by the compression of the geotextiles as a result of bentonite swelling (Tab. 4). Hence the e_m/e_M ratio
 574 did not change much in the block parts of any of the tests, except for the samples closest to the
 575 hydration surface of test CW2, where it decreased.



576

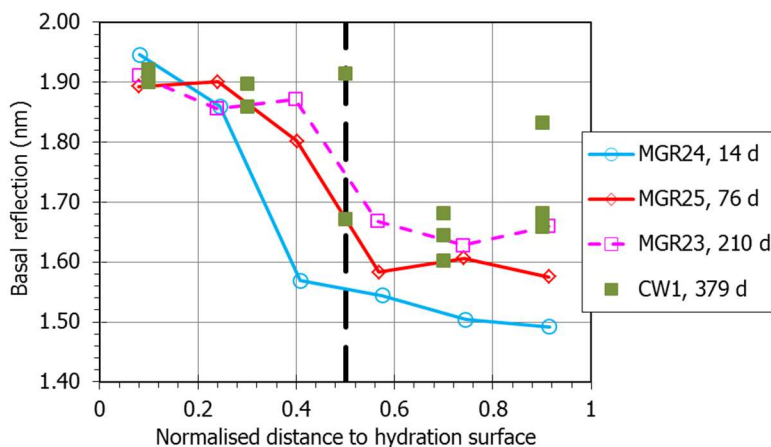
577 **Fig. 17. Void ratio corresponding to different pore sizes obtained by MIP in samples from tests CW (the thick horizontal**
 578 **lines indicate the distribution for the reference block and pellets)**

579 3.4 Interlayer space

580 The basal reflection of the subsamples after some MGR tests was determined by XRD. Fragments of
 581 the samples were X-rayed the same day in which the cells were dismantled, trying to keep the final

582 water content unchanged by avoiding any accidental drying. The results obtained showed that the
 583 (001)-reflection was a double one that could be decomposed into two diffraction peaks by profile
 584 fitting of the XRD patterns. In the case of the block samples the main diffraction peak corresponded
 585 to the full development of the 2-layer hydrate (~1.5-1.7 nm) and the secondary one to the 3-layer
 586 hydrate (~1.8-1.9 nm), whereas in the pellets samples the main diffraction peak corresponded to the
 587 full development of the 3-layer hydrate and the secondary peak was higher (2.0-2.1 nm). However,
 588 the samples from test MGR24, the shortest one, showed a single diffraction peak for the (001)-
 589 reflection at much lower values.

590 Fig. 18 shows the values corresponding to the main reflections. The initial basal reflection for the
 591 pellets samples would be ~1.3 nm, and for the compacted block ~1.5 nm. For a given test, no matter
 592 its duration, the final values were higher in the pellets part. For the pellets samples with water
 593 content higher than 30% the values were all above 1.8 nm, practically corresponding to the 3 water
 594 layer hydration state of the smectite. In contrast, block samples of similar water content had lower
 595 basal spacings.



596
 597 **Fig. 18: Main diffraction peak of the basal reflection of subsamples of MGR and CW tests (total length of 10 cm in tests**
 598 **MGR and 12 cm in CW). Hydration took place through the pellets except in tests MGR27 and CW2. The duration of the**
 599 **tests is indicated in days**

600 **3.5 Healing of block/pellets interface: gas testing**

601 At the end of the tests in transparent cell, a cylindrical subsample was obtained by drilling across the
 602 pellets/block interface to measure the gas breakthrough pressure as an indicator of the healing of
 603 the interface. These subsamples were vertically crossed by the interface (Fig. 11) and had a nominal
 604 diameter of 3.8 cm. The initial and final characteristics of the samples as well as those of the tests are
 605 shown in Tab. 5.

606 **Tab. 5. Characteristics of the samples before and after gas testing and characteristics of the tests**

| Test | CW1-gas | | CW2-gas | |
|-------------------------------|---------|-------|---------|-------|
| | Initial | Final | Initial | Final |
| ρ_d (g/cm ³) | 1.33 | 1.43 | 1.36 | 1.40 |
| h (cm) | 2.16 | 2.13 | 2.15 | 2.15 |
| ϕ (cm) | 3.78 | 3.68 | 3.79 | 3.73 |
| w (%) | 34.8 | 32.2 | 30.3 | 29.3 |
| S_r (%) | 92 | 99 | 83 | 85 |
| Confining P (MPa) | 3.0 | | 1.1-2.3 | |
| Injection P (MPa) | 0.2-2.9 | | 0.2-0.3 | |
| Duration (days) | 32 | | 4 | |

607

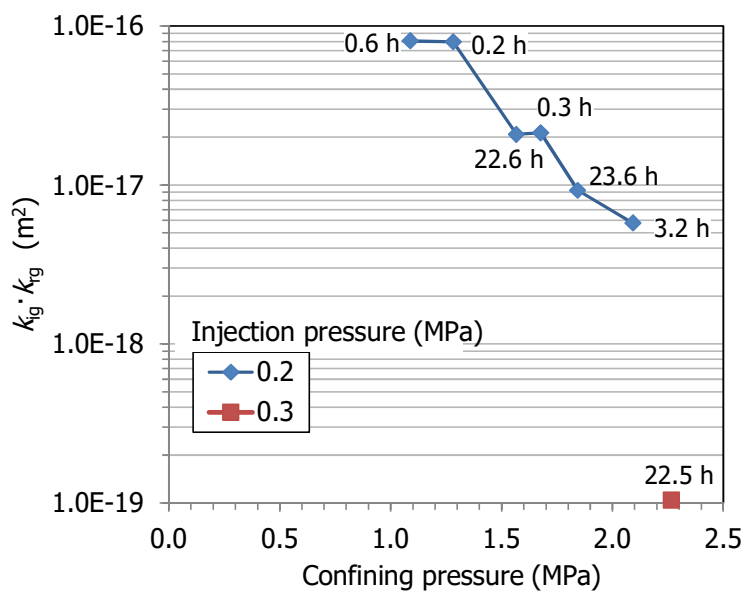
608 In test CW1-gas a confining pressure of 3 MPa was applied, corresponding to the swelling pressure of
 609 the bentonite with a dry density of 1.45 g/cm³ (the global value for test CW1) according to Equation
 610 3. This value was selected to keep approximately the same stress state as the bentonite likely had at
 611 the end of the test, when almost full saturation was reached, and prevent the interface from
 612 mechanically splitting. The injection pressure was increased 0.1 MPa every two hours, from 0.2 to
 613 2.95 MPa. There was no flow until the injection pressure reached 2.00 MPa. For injection pressures

614 from 2.00 to 2.24 MPa there were barely measurable flow pulses. There was again no flow until 2.85
615 MPa of injection pressure. For gas injection pressure of 2.90 MPa unsteady flow pulses close to the
616 turndown value of the flowmeters were detected. At the end of the test the sample had consolidated
617 as a result of the confining and gas pressure applied and its water content had slightly decreased,
618 which would indicate that some water movement took place during the test.

619 It can be considered that the gas breakthrough pressure was ~ 2.2 MPa, although no steady, correctly
620 measurable flow was measured at any moment. This breakthrough pressure would be in the order of
621 the values expected for FEBEX samples compacted to dry densities between 1.35 and 1.45 g/cm³,
622 which would be between 1.5 and 3.5 MPa (Gutiérrez-Rodrigo 2018, Gutiérrez-Rodrigo et al. 2021).

623 Because the sample from test CW2 was not saturated, the confining pressure applied during gas
624 testing was initially lower, 1.1 MPa. In this case the outflow was high from the first step of injection
625 pressure (0.2 MPa), and the confining pressure had to be increased to reduce it. Outflow continued
626 until the confining pressure was 2.3 MPa, for which pressure no flow occurred. Then the injection
627 pressure was increased to 0.3 MPa, flow resumed and the test was dismantled. The permeability
628 values obtained for each pressure step are shown in Fig. 19. They are expressed as $k_{rg} \cdot k_{ig}$, where k_{rg} is
629 the relative gas permeability and k_{ig} is the intrinsic permeability measured with gas flow. The
630 duration of the steps had some influence on the values obtained, because the sample consolidated
631 as a result of the confining pressure application, which resulted in a decrease of gas permeability.
632 This would explain the significantly lower value obtained in the last step, after the sample had been
633 submitted to a confining pressure of 2.3 MPa for one day. Indeed the sample dry density increased
634 during the test, even though the total duration of the test was of only 4 days. In particular, the
635 permeability value obtained for a confining pressure of 0.1 MPa was $8 \cdot 10^{-17}$ m². These values are
636 lower than those expected for the FEBEX bentonite compacted with similar accessible void ratio (i.e.
637 void ratio accessible for gas flow, $e(1-S_r)$, in this sample 0.165). According to the correlation
638 presented in Villar et al. (2013), for a sample of FEBEX bentonite compacted at the same accessible

639 void ratio, with no interface in it and tested under the same confining pressure, the intrinsic
 640 permeability should be $\sim 2 \cdot 10^{-15} \text{ m}^2$, i.e. considerably higher. This would indicate that the
 641 pellets/block interface was not a preferential gas pathway and flow took place through the bentonite
 642 whole porosity. Hence, the interface was perfectly healed and sealed, even though full saturation
 643 had not been reached in this area.



644
 645 **Fig. 19. Gas permeability measured in a sample from test CW2 including the interface between block and pellets. The**
 646 **duration of the steps is indicated in hours**

647 4 Discussion

648 The tests presented allowed to follow the hydro-mechanical evolution of a two-component buffer
 649 material upon hydration under isochoric conditions at ambient temperature. The two components
 650 (bentonite pellets –GBM– and bentonite block) had different initial water contents and dry densities.
 651 Except in tests MGR27 and CW2, hydration took place through the pellets part, which had a higher
 652 intrinsic permeability than the block because of its lower dry density, higher macroporosity and

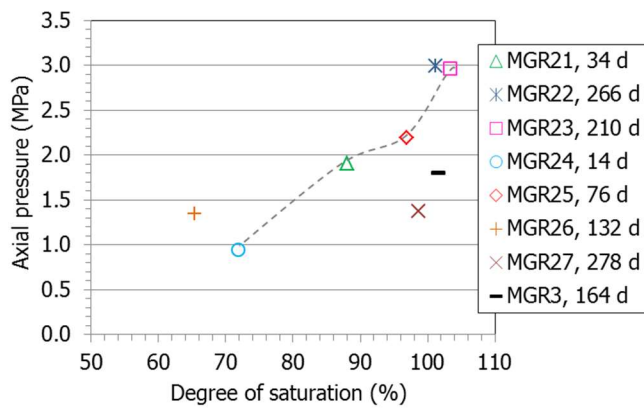
653 lower water content (Villar and Lloret 2001, Romero 2013). During the MGR tests the axial pressure
654 was measured on the sample surface opposite to hydration.

655 The pressure development was not mainly related to the quantity of water taken (i.e. to the overall
656 degree of saturation), but to the water intake rate. Thus, when hydration took place under very low
657 water inflow rate (MGR22, MGR26), the axial pressure for a given overall degree of saturation was
658 much higher than for the tests in which hydration took place more quickly (Fig. 4, right). Similarly, in
659 test MGR27, in which hydration under constant injection pressure was slower because it took place
660 through the higher-density block part, the pressure reached for a given overall degree of saturation
661 was initially (namely until the overall degree of saturation reached ~60%) higher than for the tests in
662 which saturation took place through the pellets. This suggests that it was the redistribution of water
663 in the microstructure the mechanism that triggered most of the swelling. This is supported by the
664 fact that in test MGR23 the axial pressure considerably increased during the 14-day period during
665 which inadvertently no water was supplied to the cell, showing that water redistribution inside the
666 bentonite can cause pressure increase. X-ray tomography scans of oedometer tests and image post-
667 processing, allowed Massat et al. (2016) to correlate the evolution of swelling pressure and inter-
668 aggregate porosity in compacted bentonite and conclude that water redistribution inside the
669 structure led to reaching a stable swelling pressure. In the EB in situ test performed at the Mont Terri
670 URL, where a large-scale two-component barrier (FEBEX GBM and blocks) was tested for 10.5 years,
671 most of the sensors installed in the bentonite recorded relative humidity values of 100% only one
672 year after the beginning of the test, whereas it took four years for the total pressure sensors to
673 record stable values that kept approximately constant until the end of the test (García-Siñeriz et al.
674 2015).

675 The different strength of the materials involved also played a role on the axial pressure development
676 kinetics at the first stages of saturation. When the water intake was very slow, the block part was
677 able to swell relatively quickly (see the dry density and water content distribution at the end of test

678 MGR26 in Fig. 10), and because the pellet part was comparatively dry (drier than at the end of any
679 other test) and consequently rigid, the stress was more effectively transmitted towards the top and
680 hence recorded by the load cell. In contrast, when hydration was quicker, the pellet part soon
681 collapsed and was easily compressed by the downwards swelling of the block, resulting in a lower
682 axial load measured on top. In fact, a downwards movement of the pellets/block interface in cell
683 CW1 was observed, indicating the compression (or collapse) of the pellets part. In contrast this
684 interface moved upwards in cell CW2, saturated through the block.

685 The final axial pressure measured in the tests is plotted against the final degree of saturation in Fig.
686 20. Overall the pressure consistently increased with the average degree of saturation, but in test
687 MGR26, saturated under low water inflow, a pressure higher than expected according to the trend
688 marked by the other tests was reached, consistent with the description of the initial stages of
689 saturation given in the previous paragraph. Once full saturation was reached the swelling pressure
690 was the same irrespective of the way of saturation, and thus tests MGR22 and MGR23 showed the
691 same final pressure (3 MPa). This value is higher than the swelling pressure expected for a FEBEX
692 bentonite sample compacted to the average dry density value of the MGR tests (1.45 g/cm^3). The
693 theoretical value would be $2.0 \pm 0.5 \text{ MPa}$, according to the empirical correlation between dry density
694 and swelling pressure obtained in small standard oedometers (Eq. 3). Previous researches suggested
695 that there is a scale effect on the swelling pressure measured in the laboratory, which tends to be
696 higher as the testing cell is larger (Imbert & Villar 2006).



697

698 **Fig. 20. Final axial pressures measured as a function of the final degree of saturation of MGR tests (average $\rho_d=1.45$**
 699 **g/cm^3)**

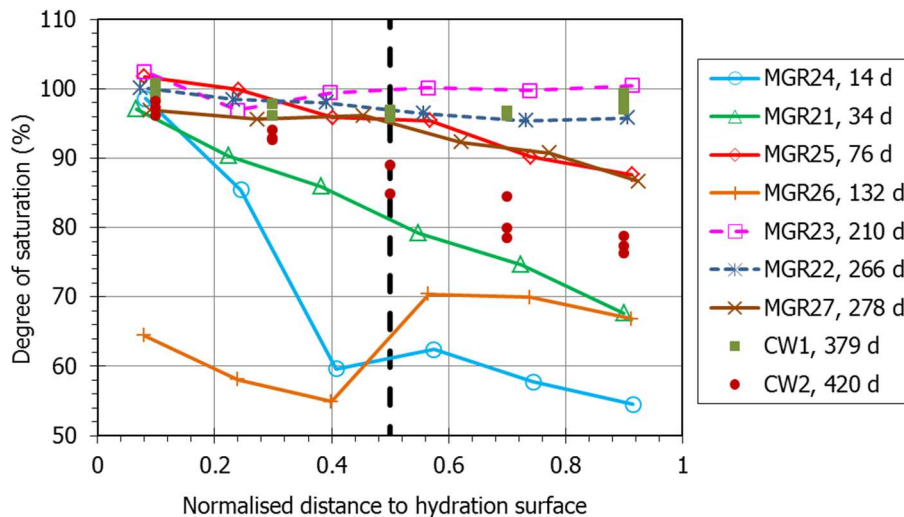
700 Even though full saturation had not been reached in test MGR27 (final $S_r=99\%$), the final pressure
 701 measured in this test was much lower than could be expected according to the general trend for
 702 tests in which saturation took place through the pellets shown in Fig. 20. Hydration tests performed
 703 in large-scale cells where radial and axial pressures were measured at different heights along the
 704 sample length showed that during saturation, the transient pressure values were related to the local
 705 dry density (Dueck et al. 2016, Baryla et al. 2019, Bian et al. 2019, Bernachy-Barbe et al. 2020,
 706 Harrington et al. 2020). In the case of test MGR27, the pellets part, on top of the sample, had the
 707 final lowest dry density (Fig. 10) and lower degree of saturation (Fig. 21). It is likely that the axial load
 708 measured reflected mainly the local pressure at the upper part of the sample, which would be lower
 709 than the pressure that would have been measured at the bottom (in the block part) if there had been
 710 a pressure sensor in the area. In other words, the axial pressure measured on top would not be fully
 711 representative of the average pressure developed by the sample, because it would also be affected
 712 by the local conditions on top of the sample (lower density and degree of saturation). Similarly, the
 713 axial top pressure measured in the rest of the tests would also be conditioned by the higher dry
 714 densities in this area, where the block was placed (Fig. 10). Hence, in addition to the scale effect

715 commented in the previous paragraph, a further reason for the higher than expected pressures
716 observed would be the influence of the higher density close to the measuring area on top.

717 As a further corroboration of that hypothesis, the final swelling pressure reached in a test performed
718 in the same oedometer with a mixture of regular-shaped FEBEX bentonite pellets and powder in a
719 70/30 ratio has also been included in the Figure (test MGR3). The average dry density of this mixture
720 was 1.45 g/cm^3 (as in the MGR tests presented here) and the initial water content 13.6% (Villar
721 1999). In this case the swelling pressure of the saturated sample had an intermediate value between
722 the trend for tests having the pellets on top and the test with the block on top (MGR27). This would
723 reflect the intermediate value of dry density on the top part of the sample, which was 1.43 g/cm^3 at
724 the end of test MG3, 1.46 g/cm^3 at the end of tests MGR22 and MGR23 and 1.42 g/cm^3 at the end of
725 test MGR27, which in addition was less saturated.

726 The tests performed by Martikainen et al. 2018 (reported in Talandier, 2019) were very similar in
727 design and dimensions to the tests presented here, with hydration under an injection pressure of 10
728 kPa taking place through the pellets (hence comparable to tests MGR21, MGR23 to MGR25).
729 Hydration took place through the top surface, where the pellets were placed. In these tests MX-80
730 bentonite was used and the radial pressure developed by the block and the pellets parts were
731 measured in addition to the axial ones. The axial and radial pressure development in the areas
732 farther away from hydration (i.e. around the block part) displayed the initial peak followed by a
733 decrease and a smooth eventual increase observed in some MGR tests (Fig. 4). These measurements
734 also showed significantly lower pressures in the pellets than in the block part. The modelling groups
735 involved in a benchmark where these tests were analysed, concluded that this difference was due to
736 the initial contrast of density between the top and bottom of the sample but also to the friction
737 between the bentonite and the steel cell wall (Talandier, 2019).

738 Indeed none of the tests reached a final complete homogeneity in terms of dry density or water
 739 content: the water content decreased from the hydration surface upwards whereas the dry density
 740 increased (Fig. 10). These heterogeneities resulted from the initial swelling and resulting density
 741 decrease of the bentonite that became first saturated (those parts closest to the bottom hydration
 742 surface), and the consequent compression of the bentonite located upwards. In contrast, a final
 743 homogeneous degree of saturation close to 100% was reached in the longer tests saturated through
 744 the pellets, i.e. MGR22, MGR23 and CW1 (Fig. 21). Once overall full saturation was reached, no
 745 further water content or dry density changes are to be expected, which would mean that part of the
 746 initial volume changes were irreversible. Also in the large-scale EB test mentioned above, no spatial
 747 trends were found for the degree of saturation, despite the fact that density and water content
 748 gradients remained (García-Siñeriz et al. 2015). In all cases the pellets/block interface did not seem to
 749 have any effect on the continuous gradients observed, i.e. there were no sudden changes across the
 750 interface.



751
 752 **Fig. 21. Final degree of saturation along the samples of MGR and CW tests (total length of 10 cm in tests MGR and 12 cm**
 753 **in CW). Hydration took place through the pellets except in tests MGR27 and CW2. The duration of the tests is indicated in**
 754 **days**

755 The two tests in which hydration took place through the block (MGR27 and CW2) were far from full
756 saturation, despite the fact that they were the longest ones performed in each kind of cell. It is
757 remarkable that in all the tests the area closest to the hydration surface was fully saturated, except in
758 test MGR26. This test, performed under constant flow and lasting 132 days, did not follow the overall
759 trend, since the increase in water content was moderate and similar for both halves, attesting the
760 more homogeneous water redistribution allowed by slow hydration. Vapour diffusion in the pore
761 spaces would be the water transfer mechanism away from the hydration surface, as postulated by
762 Kröhn (2005), who described the time-dependent water content distribution during the saturation of
763 compacted bentonite under laboratory conditions by Fick's second law. Eventually, when full
764 saturation was reached, the differences in the physical state of samples saturated under constant
765 pressure or flow obliterated, resulting in the similar water content and dry density distribution
766 patterns of tests MGR22 and MGR23.

767 Concerning the microstructural modifications during hydration, the GBM and the block parts
768 behaved quite differently and in fact most parameters inferred by MIP (volume and size of each pore
769 range, ratio between them), were different for the two components of the samples. Unlike the
770 physical variables discussed in the previous paragraphs, in most tests there was not a smooth change
771 between the microstructural parameters of pellets and block. The most notable change in the pellets
772 parts was the disappearance of the pores larger than 550 μm and the overall drastic decrease in size
773 and volume of macropores. In contrast, the mean size of the pores smaller than 200 nm increased
774 with respect to the original values for all the pellets subsamples. This was also the case for the block
775 samples. Furthermore, in the block subsamples the volume and size of the macropores tended to
776 increase, except in the shorter, less saturated tests. The increase of both e_m and e_M in the blocks
777 subsamples resulted from the overall decrease in dry density experienced by the block upon
778 hydration. Nevertheless, the e_m/e_M ratio increased from the initial ~ 0.3 to values higher than 0.7 in all
779 samples, but much more significantly in the pellets samples. Only the driest pellets samples

780 (corresponding to the shorter tests, test MGR26 performed under constant flow, and test CW2
781 saturated through the block) had e_m/e_M ratios close to the initial one. These samples kept also pores
782 larger than 550 μm that cannot be detected by MIP (because of the technique limitations) but were
783 inferred as explained at the beginning of section 3.3. Pores larger than $\sim 70 \mu\text{m}$ were actually
784 observed by MIP in some pellets samples of test CW2 (Fig. 16), where the pellets part was not
785 completely saturated. Closing of large voids (or very low density areas filled by powder) between
786 regular-shaped bentonite pellets upon hydration was observed by X-ray computed tomography by
787 van Geet et al. (2005), Molinero et al. (2018) and Reijonen et al. (2020), among others.

788 The only sample that kept quite homogeneous values across the pellets/block interface, in terms of
789 e_m , e_M and mean pore sizes, was that from test MGR27. This was also the test reaching a highest
790 homogeneity concerning dry density and water content, which suggests that the microstructural
791 changes were related to the changes in dry density and water content and thus to temporal
792 evolution.

793 Hence, as a result of hydration the volume of micropores increased in all the bentonite with respect
794 to the initial one, particularly in the case of the pellets. The increase in the volume of micropores was
795 likely related to the increase in the smectite basal spacing as a result of the hydration of the
796 interlayer cations (Fig. 18), which is the driving mechanism for crystalline swelling, predominant in
797 compacted bentonite saturated under isochoric conditions (e.g. Pusch et al. 1990, Devineau et al.
798 2006). Holmboe et al. (2012) determined by XRD profile fitting that in bentonite samples saturated
799 under confined conditions the interlayer porosity dominated total porosity and for dry densities 1.4-
800 1.8 g/cm^3 the interparticle porosity was $\leq 3\%$. As it happened with the pore size distribution obtained
801 by MIP, the basal spacings were clearly distinct for pellets and block samples. In contrast, the basal
802 spacings determined in wet samples from the in situ EB experiments (using the same procedure and
803 methodology as in this work) did not show clear differences between block and pellets (Villar et al.
804 2014). Since the samples from the in situ test were matured for 10.5 years, it could be expected that

805 in the long term, also the microstructure of the two components of the much shorter MGR tests
806 would become homogenised. In samples from the in situ test –which were fully saturated– the basal
807 spacings indicated that 3 water layers were completely developed in the interlayer (values around
808 1.85 nm). For water contents below ~38%, the basal spacing increased with the water content, but
809 for higher values the basal spacing was quite constant, irrespective of the water content, which was
810 also observed in the samples from the MGR tests.

811 **5 Conclusions**

812 The hydro-mechanical evolution of a two-component bentonite buffer material –low density pellets
813 mixtures and higher density compacted blocks– was studied by means of a series of laboratory
814 hydration tests performed under isochoric conditions. The tests were performed in a large-scale
815 oedometer (10x10 cm) and in a transparent cell (12x12x2 cm). In the first case the axial pressure was
816 measured on the sample surface opposite to hydration. In most tests hydration took place through
817 the pellets part, but the effect of hydrating through the block was also checked. As well, tests were
818 performed either under a low water injection pressure or under a low water inflow rate.

819 The analysis of the results obtained allowed to draw the following conclusions:

- 820 – Because of their low density and large macroporosity, hydration through the pellets was initially
821 quick, even though the water injection pressure was very low.
- 822 – The way of hydration conditioned the water intake and the pressure development kinetics. Slow
823 hydration (e.g. under a controlled low flow of through the block) delayed the start of pressure
824 development, but allowed higher pressures to be reached for lower overall degrees of
825 saturation. The reason could be the longer time available for water redistribution from the
826 macropores to the microstructure (particularly the montmorillonite interlayer), which would be
827 the responsible for swelling. The interplay between the different strengths of the two

828 components may also be a relevant factor on the axial load measured at the first stages of
829 saturation.

830 – Irrespective of the way of saturation (constant flow or pressure), the pressure development was
831 not continuous. After a first sharp increase (which was quicker under constant pressure), there
832 was an intermediate period of pressure stabilisation. Only when the overall degree of saturation
833 was very high, the pressure increased again until its final equilibrium value. This pressure
834 development pattern had been previously observed also in samples of compacted bentonite and
835 of pellets.

836 – The stress measuring devices (in this case an external load cell on top of the oedometer cover)
837 reflect local stresses which are conditioned by the local dry density. Hence, when the block part
838 was on top, the final pressure value of the saturated sample was higher than the value expected
839 for smaller samples of bentonite compacted at the same average dry density. When the pellet
840 part was on top, the contrary happened. Friction between the bentonite and the cell steel wall
841 could also contribute to these differences. This research has put forward the necessity of using
842 testing devices in which pressure can be measured at different locations to correctly assess the
843 stress state of inhomogeneous samples.

844 – Bentonite water content and dry density gradients were observed at the end of the tests. For a
845 given hydration rate they were dependent on the hydration time and, although they attenuated
846 over time, they persisted even after full saturation was reached. Saturation under very low water
847 inflow rate (either imposed or resulting from the low permeability of the block part when
848 saturation took place through it) resulted in more uniform water contents and smoother
849 gradients, also in terms of pore sizes.

850 – In contrast, the microstructure of the bentonite in the two components was very different even
851 after full saturation. Despite of the drastic reduction in the volume and size of macropores in the
852 pellets parts, they continued to be higher than in the block part and consequently the e_m/e_M was

853 lower in the pellets part. The basal spacing of the smectite, which is an indication of the number
854 of water layers in the interlayer, was higher in pellets samples than in block samples. However,
855 an overall trend to pore size homogenisation towards smaller sizes over time was observed.
856 – The water content and dry density gradients were not affected by the pellets/block interface.
857 After full saturation the pellets/block interface was impervious to gas.

858 The behaviour of a two-component barrier can be affected by the particular dry density and water
859 content of each barrier component as well as their size and geometry, and by the boundary
860 conditions, such as the existence of gaps, temperature and water salinity and availability. This
861 research has just analysed the effect of geometry and water availability, but there are not systematic
862 published researches having analysed all the other aspects yet.

863 The evidence provided by these experimental results along with the outcomes of the large-scale EB
864 test, in which a similar two-component barrier was tested for 10.5 years, suggests that, although the
865 initial heterogeneity of the barrier system and the deformations induced in the first stages of
866 saturation tend to attenuate over time, residual inhomogeneities will persist and remain even after
867 full saturation. The kind and extent of these heterogeneities will depend on the initial and boundary
868 conditions of the barrier.

869

870 **Acknowledgements**

871 The research leading to these results was financed by the Beacon project, which receives funding
872 from the Euratom Research and Training Programme 2014–2018 under grant agreement number
873 745942. Part of the laboratory work was carried out by J. Aroz. Dr. Pedro Luis Martín of CIEMAT
874 contributed to the design of the tests in transparent cell. The mercury intrusion porosimetry tests
875 were performed at the Petrophysical laboratory of CIEMAT by N. Brea. The XRD measurements were
876 performed at the High-Level Radioactive Waste Unit of CIEMAT and at the Unidad de Técnicas

877 Geológicas del CAI de Ciencias de la Tierra y Arqueometría of the Universidad Complutense de
878 Madrid. L. Gutiérrez-Nebot (CIEMAT) performed the XRD interpretation. Beatriz Carbonell was hired
879 in the framework of the Spanish National System of Youth Guarantee in R+D 2014, with financing of
880 the European Social Fund and the Youth Employment Initiative.

881

882 **CRedit statements**

883 **M.V. Villar:** conceptualization, formal analysis, investigation, writing, editing, supervision

884 **R.J. Iglesias:** investigation, formal analysis, resources, visualization, review

885 **C. Gutiérrez-Álvarez:** investigation, formal analysis, resources, visualization, review

886 **B. Carbonell:** investigation, formal analysis, resources, visualization, review

887

888 **6 References**

889 Abed, A., Solowski, W.T. 2019. Simulation of swelling pressure evolution during infiltration in a
890 bentonite block-pellet laboratory scale test. Japanese Geotechnical Society Special
891 Publication 7(2): 323-330. DOI: 10.3208/jgssp.v07.052

892 Alcantara A, Romero E., Mokni N., Olivella S. 2020. Microstructural and hydro-mechanical behaviour
893 of bentonite pellets and powder mixtures. E-UNSAT 2020. E3S Web of Conferences 195,
894 04003. <https://doi.org/10.1051/e3sconf/202019504003>

895 Baryla, P., Bernachy-Barbe, F., Bosch, J.A., Campos, G., Carbonell, B., Daniels, K.A., Ferrari, A., Guillot,
896 W., Gutiérrez-Álvarez, C., Harrington, J.F., Iglesias, R.J., Kataja, M., Mašín, D., Najser, J.,
897 Rinderknecht, F., Schäfer, T., Sun, H., Tantt, J., Villar, M.V., Wiczonek, K. 2019. Bentonite

898 mechanical evolution – experimental work for the support of model development and
899 validation. DELIVERABLE (D4.1/2). Report. 132 pp.

900 Bernachy-Barbe, F., Conil, N., Guillot, W., Talandier, J. 2020. Observed heterogeneities after
901 hydration of MX-80 bentonite under pellet/powder form. Applied Clay Science 189: 105542.
902 <https://doi.org/10.1016/j.clay.2020.105542>

903 Bernachy-Barbe, F. 2021. Homogenization of bentonite upon saturation: Density and pressure fields.
904 Applied Clay Science 209: 106122. <https://doi.org/10.1016/j.clay.2021.106122>

905 Bian, X., Cui, Y.J., Zeng, L.L., Li, X.Z. 2019. Swelling behavior of compacted bentonite with the
906 presence of rock fracture. Engineering Geology 254: 25-33.
907 <https://doi.org/10.1016/j.enggeo.2019.04.004>

908 Bosgiraud, J.M., Foin, R. 2016. Test report on FSS metric clayish material emplacement tests with
909 clayish material definition and laboratory work on its performance. Project DOPAS Work
910 Package 3 - Deliverable 3.7. European Commission Grant Agreement No. 323273. 35 pp.
911 <https://igdtp.eu/documents/>

912 Devineau, K., Bihannic, I., Michot, L., Villiéras, F., Masrouri, F., Cuisinier, O., Fragneto, G., Michau, N.,
913 2006. In situ neutron diffraction analysis of the influence of geometric confinement of
914 crystalline swelling of montmorillonite. Applied Clay Science 31 (1–2): 76–84.
915 <https://doi.org/10.1016/j.clay.2005.08.006>

916 Dixon, D., Chandler, N., Graham, J., Gray, M.N., 2002. Two large-scale sealing tests conducted at
917 atomic energy of Canada's underground research laboratory: the buffer-container
918 experiment and the isothermal test. Canadian Geotechnical Journal 39: 503–518.
919 <https://doi.org/10.1139/t02-012>

920 Dueck, A., Goudarzi, R., Börgesson, L. 2016. Buffer homogenisation. Status report 3. Technical Report
921 SKB TR-16-04. Svensk Kärnbränslehantering, Stockholm, 104 pp.

922 ENRESA 2005. Engineered barrier emplacement experiment in Opalinus Clay for the disposal of
923 radioactive waste in underground repositories. Final Report. Publicación Técnica ENRESA
924 02/05. Madrid, 101 pp.

925 ENRESA 2006. FEBEX Full-scale Engineered Barriers Experiment, Updated Final Report 1994–2004.
926 Publicación Técnica ENRESA 05-0/2006, Madrid, 590 pp.

927 Gaus, I., Garitte, B., Senger, R., Gens, A., Vasconcelos, R., García-Sineriz, J.L., Trick, T., Wieczorek, K.,
928 Czaikowski, O., Schuster, K., Mayor, J.C., Velasco, M., Kuhlmann, U., Villar, M.V. 2014. The HE-
929 E Experiment: Lay-out, Interpretation and THM Modelling. Nagra Arbeitsbericht NAB 14-53.
930 Wettingen, 140 pp.

931 Gens, A., Alcoverro, J., Blaheta, R., Hasal, M., Michalec, Z., Takayama, Y., Lee, C., Lee, J., Kim, G.Y.,
932 Kuo, W.J., Lin, C.Y. 2021. HM and THM interactions in bentonite engineered barriers for
933 nuclear waste disposal. International Journal of Rock Mechanics and Mining Sciences 137:
934 104572. <https://doi.org/10.1016/j.ijrmms.2020.104572>

935 Gutiérrez-Rodrigo, V. 2018. Transporte de gas en materiales de barrera. Tesis Doctoral. Universidad
936 Complutense de Madrid. Colección Documentos CIEMAT. ISBN: 978-84-7834-802-2. Madrid,
937 303 pp.

938 Gutiérrez-Rodrigo, V., Martín, P.L., Villar, M.V. 2021. Effect of interfaces on gas breakthrough pressure
939 in compacted bentonite used as engineered barrier for radioactive waste disposal. Process
940 Safety and Environmental Protection 149: 244-257.
941 <https://doi.org/10.1016/j.psep.2020.10.053>.

942 Grambow, B. 2016. Geological disposal of radioactive waste in clay. *Elements* 12: 239-245. DOI:
943 10.2113/gselements.12.4.239

944 Harrington, J.F., Daniels, K.A., Wiseall, A.C., Sellin, P., 2020. Bentonite homogenisation within
945 engineered cavities: the evolution of swelling pressure during bentonite hydration.
946 *International Journal of Rock Mechanics and Mining Sciences* 136, 104535.
947 doi:10.1016/j.ijrmms.2020.104535.

948 Hoffmann, C. 2005. Caracterización hidromecánica de mezclas de pellets de bentonita. Estudio
949 experimental y constitutivo. (PhD Thesis), Universitat Politècnica de Catalunya, Barcelona,
950 387 pp.

951 Hoffmann, C., Alonso, E.E. and Romero, E. 2007. Hydro-mechanical behaviour of bentonite pellet
952 mixtures. *Physics and Chemistry of the Earth* 32: 832-849.
953 <https://doi.org/10.1016/j.pce.2006.04.037>

954 Holmboe, M., Wold, S., Jonsson, M. 2012. Porosity investigation of compacted bentonite using XRD
955 profile modeling. *Journal of Contaminant Hydrology* 128: 19-32.
956 doi:10.1016/j.jconhyd.2011.10.005

957 Imbert, C., Villar, M.V. 2006. Hydro-mechanical response of a bentonite pellets/powder mixture upon
958 infiltration. *Applied Clay Science* 32: 197-209. <https://doi.org/10.1016/j.clay.2006.01.005>

959 Imbert, C., Gatabin, C., Maugis, P., Leboulch, D., Mouche, E. 2002. Hydro-mechanical behaviour of a
960 heterogeneous swelling clay material. In: Auriault, J.L., Block, J.F., Geindreau, C., Royer, P.
961 Bloch, J.F., Boutin, C., Lewandowska, J. (Eds.) *Poromechanics II: Proceedings of the Second*
962 *Biot Conference on Poromechanics, Grenoble*. Swets & Zeitlinger, Balkema, Lisse. 225-230.

963 Kennedy, K., Verfuss, F., Plötze, M. 2004. Engineered Barrier Emplacement (EB) Experiment in
964 Opalinus Clay: Granular material backfill product documentation. EC contract FIKW-CT-2000-
965 00017. Project Deliverable D3c. Mont Terri Technical Note 2004-17, 61 pp.

966 Kröhn, K.P. 2005. New evidence for the dominance of vapour diffusion during the re-saturation of
967 compacted bentonite. *Engineering Geology* 82: 127-
968 132. <https://doi.org/10.1016/j.enggeo.2005.09.015>

969 Lloret A., Villar M.V., Sánchez M., Gens A., Pintado X., Alonso E.E. 2003. Mechanical behaviour of
970 heavily compacted bentonite under high suction changes. *Géotechnique* 53 (1): 27-40.
971 <https://doi.org/10.1680/geot.53.1.27.37258>

972 Martikainen, J., Pintado, X., Mamunul, H. 2018. Laboratory tests to evaluate bentonite
973 homogenization. Internal memorandum POS-026579. Eurajoki, Finland: Posiva Oy.

974 Mašín, D. 2013. Double structure hydromechanical coupling formalism and a model for unsaturated
975 expansive clays. *Engineering Geology* 165: 73-88.
976 <https://doi.org/10.1016/j.enggeo.2013.05.026>

977 Massat, L., Cuisinier, O., Bihannic, I., Claret, F., Pelletier, M., Masrouri, F., Gaboreau, S. 2016. Swelling
978 pressure development and inter-aggregate porosity evolution upon hydration of a
979 compacted swelling clay. *Applied Clay Science* 124–125: 197-210.
980 <https://doi.org/10.1016/j.clay.2016.01.002>

981 Molinero Guerra, A. 2018. Caractérisations expérimentale et numérique du comportement hydro-
982 mécanique d'un matériau hétérogène : mélange de poudre/pellets de bentonite. Ph. Thesis,
983 Université Paris-Est. 190 pp.

984 Molinero Guerra, A., Cui, Y.-J., Mokni, N., Delage, P., Bornert, M., Aïmedieu, P., Tang, A.M., Bernier F.
985 2018. Investigation of the hydro-mechanical behaviour of a pellet/powder MX80 bentonite

986 mixture using an infiltration column. *Engineering Geology* 243: 18-25.
987 10.1016/j.enggeo.2018.06.006

988 Müller, H.R., Garitte, B., Vogt, T., Köhler, S., Sakaki, T., Weber, H., Spillmann, T., Hertrich, M., Becker,
989 J.K., Giroud, N., Veerle, C., Diomidis, N. Vietor, T. 2017. Implementation of the full-scale
990 emplacement (FE) experiment at the Mont Terri rock laboratory. *Swiss Journal of*
991 *Geosciences* 110: 287–306. DOI 10.1007/s00015-016-0251-2

992 NAGRA 2019. Implementation of the Full-scale Emplacement Experiment at Mont Terri: Design,
993 Construction and Preliminary Results. NAGRA Technical Report NTB 15-02. Wettingen, 147
994 pp.

995 Navarro, V., Asensio, L., Morena, G. de la, Gharbieh, H., Alonso, J., Pulkkanen, V.M. 2020. From
996 double to triple porosity modelling of bentonite pellet mixtures. *Engineering Geology* 274:
997 105714. <https://doi.org/10.1016/j.enggeo.2020.105714>

998 Pusch, R., Karnland, O., Hökmark, H. 1990. GMM -A general microstructural model for qualitative and
999 quantitative studies on smectite clays. SKB Technical Report TR 90-43. Stockholm, 94 pp.

1000 Reijonen, H.M., Kuva, J., Heikkilä, P. 2020. Benefits of applying X-ray computed tomography in
1001 bentonite based material research focussed on geological disposal of radioactive waste.
1002 *Environmental Science and Pollution Research* 27: 38407–38421.
1003 <https://doi.org/10.1007/s11356-020-08151-2>

1004 Romero, E. 2013. A microstructural insight into compacted clayey soils and their hydraulic properties.
1005 *Eng. Geol.* 165: 3-19. <http://dx.doi.org/10.1016/j.enggeo.2013.05.024>

1006 Salo, J.P., Kukkola, T. 1989. Bentonite pellets, an alternative buffer material for spent fuel canister
1007 deposition holes. Workshop “Sealing of Radioactive Waste Repositories”. Braunschweig.

1008 Sánchez M, Gens A, Guimarães L, Olivella, S, 2005. A double structure generalized plasticity model for
1009 expansive materials. *International Journal for Numerical and Analytical Methods in*
1010 *Geomechanics* 29: 751–787. DOI:10.1002/nag.434.

1011 Sellin, P., Leupin, O., 2013. The use of clays as an engineered barrier in radioactive-waste
1012 management – a review. *Clays and Clay Minerals* 61 (6): 477–498.
1013 <https://doi.org/10.1346/CCMN.2013.0610601>

1014 Sing, K.S.W., Everett, D.H., Haul, R.A.W., Moscou, L., Pierotti, R.A., Rouquérol, J., Siemieniowska, T.
1015 1985. Reporting physisorption data for gas/solid systems with special reference to the
1016 determination of surface area and porosity. *Pure and Applied Chemistry* 57(4): 603-619.
1017 IUPAC.

1018 SKB. 2010. Buffer, Backfill and Closure Process Report for the Safety Assessment SR-Site. TR-10-47.
1019 Swedish Nuclear Fuel and Waste Management Co (SKB), Stockholm, 360 pp.

1020 Talandier, J. (Ed.) 2019. Synthesis of results from task 5.1. BEACON Deliverable D5.1.2. 334 pp.

1021 Van Geet, M., Volckaert, G., Roels, S. 2005. The use of microfocus X-ray computed tomography in
1022 characterising the hydration of a clay pellet/powder mixture. *Applied Clay Science* 29 (2): 73-
1023 87. <https://doi.org/10.1016/j.clay.2004.12.007>

1024 Van Geet, M., Bastiaens, W., Volckaert, G., Weetjens, E., Sillen, X., Maes, N., Imbert, C., Billaud, P.,
1025 Touzé, G., Filippi, M., Plas, F., Villar, M. V., García-Gutiérrez, M., Mingarro, M., Gens, A.,
1026 Vallejan, B. 2009. RESEAL II. A large-scale in situ demonstration test for repository sealing in
1027 an argillaceous host rock - Phase II. Final report.: EUR 24161, Nuclear Science and
1028 Technology, European Commission, Luxembourg, 288 pp.

1029 Villar, M.V. 1999. RESEAL Project. Topical Report on Laboratory Tests. Version 1. Informe Técnico
1030 CIEMAT/DIAE/54121/2/99. Madrid, 33 pp.

- 1031 Villar, M.V. 2002. Thermo-hydro-mechanical characterisation of a bentonite from Cabo de Gata. A
1032 study applied to the use of bentonite as sealing material in high level radioactive waste
1033 repositories. Publicación Técnica ENRESA 01/2002, Madrid, 258 pp.
- 1034 Villar, M.V. 2012. EB experiment. Laboratory infiltration tests report. PEBS Deliverable D2.1-5.
1035 CIEMAT Technical Report CIEMAT/DMA/2G210/03/2012. 33 pp. [https://www.pebs-
1036 eu.de/PEBS/EN/Downloads/D2_1_5_pdf.pdf?_blob=publicationFile&v=1](https://www.pebs-eu.de/PEBS/EN/Downloads/D2_1_5_pdf.pdf?_blob=publicationFile&v=1)
- 1037 Villar, M.V.(Ed). 2017. FEBEX-DP Postmortem THM/THC Analysis Report. NAB 16-017. 143 pp.
- 1038 Villar, M.V., Lloret, A. 2001. Variation of the intrinsic permeability of expansive clays upon saturation.
1039 In: Adachi, K., Fukue, M. (Eds.): Clay Science for Engineering. A.A. Balkema, Rotterdam, pp.
1040 259–266.
- 1041 Villar, M.V., Gómez-Espina, R. 2012. Long-term Performance of Engineered Barrier Systems PEBS.
1042 Permeability tests in samples from the EB experiment at Mont Terri (Borehole EB-B1).
1043 Technical Note CIEMAT/DMA/2G210/06/12. Madrid, 15 pp.
- 1044 Villar, M.V.; Gutiérrez-Rodrigo, V.; Martín, P.L.; Romero, F.J. & Barcala, J.M. 2013. Gas transport in
1045 bentonite. Informes Técnicos CIEMAT 1301. Madrid, 63 pp. DOI:
1046 10.13140/RG.2.2.14334.28489
- 1047 Villar, M.V., Campos, R., Gutiérrez-Nebot, L. 2014. EB experiment. Laboratory post-mortem analyses
1048 report. PEBS Project Deliverable D2.1-7. CIEMAT Technical Report
1049 CIEMAT/DMA/2G210/01/2014. Madrid, 34 pp.
- 1050 Villar, M.V., Iglesias, R.J., Gutiérrez-Álvarez, C., Carbonell, B., Campos, R., Campos, G., Martín, P.L.,
1051 Castro, B. 2018. FEBEX-DP: Thermo-hydro-mechanical postmortem analysis of bentonite
1052 performed at CIEMAT. Technical report CIEMAT/DMA/2G216/2/16. NAB16-024. Madrid, 134
1053 pp.

1054 Villar, M.V., Campos, G., Gutiérrez-Nebot, L., Arroyo, X. 2019. Effect of prolonged drying at high
1055 temperature on the water retention capacity of bentonite (FEBEX-DP samples). *Applied Clay*
1056 *Science* 182: 105290. <https://doi.org/10.1016/j.clay.2019.105290>

1057 Villar, M.V., Iglesias, R.J., García-Siñeriz, J.L., Lloret, A., Huertas, F. 2020. Physical evolution of a
1058 bentonite buffer during 18 years of heating and hydration. *Engineering Geology* 264: 105408.
1059 <https://doi.org/10.1016/j.enggeo.2019.105408>

1060 Villar, M.V., Carbonell, B., Martín, P.L., Gutiérrez-Álvarez, C. 2021. The role of interfaces in the
1061 bentonite barrier of a nuclear waste repository on gas transport. *Engineering Geology* 286:
1062 106087. <https://doi.org/10.1016/j.enggeo.2021.106087>

1063 Volckaert, G., Bernier, F., Alonso, E., Gens, A., Samper, J., Villar, M.V., Martín, P.L., Cuevas, J.,
1064 Campos, R., Thomas, H.R., Imbert, C., Zingarelli, V. 1996. Thermal-hydraulic-mechanical and
1065 geochemical behaviour of the clay barrier in radioactive waste repositories (model
1066 development and validation). *Nuclear science and technology*. EUR 16744. Commission of
1067 the European Communities, Luxembourg, 722 pp.

1068 Volckaert, G., Dereeper, B., Put, M., Ortiz, L., Gens, A., Vaunat, J., Villar, M.V., Martín, P.L., Imbert, C.,
1069 Lassabatère, T., Mouche, E., Cany, F. 2000. A large-scale in situ demonstration test for
1070 repository sealing in an argillaceous host rock. Reseal project – Phase I. EUR 19612.
1071 Commission of the European Communities, Luxembourg, 273 pp.

1072 Yuan, S., Liu, X., Romero, E., Delage, P., Buzzi, O. 2020. Discussion on the separation of macropores
1073 and micropores in a compacted expansive clay. *Géotechnique Letters* 10: 1–7.
1074 <https://doi.org/10.1680/jgele.20.00056>

1075